EXPERIMENTAL INVESTIGATION OF A HYBRID THERMAL MANAGEMENT SYSTEM FOR AN ELECTRIC VEHICLE BATTERY MODULE

A Thesis Submitted to the
Graduate School of İzmir Institute of Technology
in Partial Fulfilment of the Requirements for the Degree of

DOCTOR OF PHILOSOPHY

in Mechanical Engineering

by
Turgay COŞKUN

June 2022
İZMİR

ACKNOWLEDGMENTS

I would never have been able to complete my thesis without the guidance of my supervisor, my thesis committee members, help from friends, and support from my family.

I would like to thank my supervisor, Prof. Dr. Erdal ÇETKİN for his excellent guidance, precious advice, patience, encouragement and immense knowledge. I would like to express my graduate to my thesis monitoring members Assoc. Prof. Dr. Murat BARIŞIK and Assist. Prof. Dr. Hasan ÇELİK for their helps and suggestions during the thesis monitoring meetings. Also, I would like to thank my thesis defence examining committee members Prof. Dr. Aytunç EREK, Assoc. Prof. Dr. M.Akif EZAN and Assoc. Prof. Dr. Ziya Haktan KARADENİZ for their valuable suggestions and encouragements.

I would like to acknowledge the financial support received from Izmir Institute of Technology within the "Scientific Research Project" (BAP-2020İYTE0027).

I would like to thank to my dear friend Sinan GÖÇMEN for his help and supports.

Lastly, I would like to thank to my dear wife Bilge COŞKUN, my son Mehmet COŞKUN and my family for their patience, motivation, and continuous support.

ABSTRACT

EXPERIMENTAL INVESTIGATION OF A HYBRID THERMAL MANAGEMENT SYSTEM FOR AN ELECTRIC VEHICLE BATTERY MODULE

Environmental concerns and limited energy sources of the world are driving force in electric vehicle technology improvements. One of the main components of the electric vehicles is battery cell. Using batteries in electric vehicles brings up new concerns such as safety problems, limit of range and so on. The temperature of the battery cell increases during charging/discharging and operation. There is an optimal temperature range (15ºC ─ 35ºC) for battery cells to maximize efficiency and prevent safety issues. The high temperature values in the battery cells can be result with fire and explosion. In addition, the performance of the battery cells is highly affected by operating temperatures. Therefore, thermal management of the battery cells is a necessity to overcome safety issues and maximize the battery performance. The feasibility of microchannel heat sink for battery cooling is investigated numerically and it is decided to continue with conventional length scales because of the higher pressure drop values in micro scales. Thus, a hybrid cooling system, using air and liquid solely or simultaneously, is developed and is introduced to a battery module. The battery module created by connecting three lithium-ion pouch cells in serial. According to the results, air cooling gives the more homogeneous temperature distribution. The lowest temperature values are observed in hybrid cooling system and temperature difference between the cells are reduced by 30% when compared to the water-cooling system. The temperature profile in air cooling shows that any increase in the ambient temperature (23ºC) or discharge rate will undergo a temperature rise in battery cells and optimal temperature ranges will be exceeded in that case. A step function, in a sequence of various discharge rate, is introduced to the battery module to determine cooling capacity of the air system during operation. The result show that the temperature of the cells is kept below 30ºC. The hybrid cooling is enabled to select cooling systems for the battery module with respect to operating condition; hence, the efficiency of the system is increased.

Keywords and Phrases: Battery Module, Lithium-ion Cells, Hybrid Cooling

ÖZET

ELEKTRİKLİ ARAÇ PİL MODÜLÜ İÇİN HİBRİT ISIL YÖNETİM SİSTEMİNİN DENEYSEL OLARAK İNCELENMESİ

Çevresel kaygılar ve sınırlı enerji kaynakları, elektrikli araçlardaki gelişmelerin temel kaynağıdır. Elektrikli araçların ana bileşenlerinden bir tanesi pil hücresidir. Elektrikli araçlarda pil kullanımı güvenlik sorunları, menzil sınırı vb. yeni endişeleri de beraberinde getirmektedir. Pil hücrelerinin sıcaklığı, şarj, deşarj ve kullanım esnasında artmaktadır. Verimliliği en üst düzeye çıkarmak ve güvenlik sorunlarını önlemek açısından pil hücreleri için belirlenmiş optimum çalışma sıcaklık aralığı (15ºC ─ 35ºC) vardır. Pil hücrelerindeki yüksek sıcaklık değerleri yangın ve patlama ile sonuçlanmaktadır. Ayrıca pil hücrelerinin performansı sıcaklık değerlerinden yüksek oranda etkilenmektedir. Bu durum, güvenlik sorunlarının üstesinden gelmek ve pil performansını en üst düzeye çıkarmak için bir termal yönetim sisteminin gerekliliğini göstermektedir. Pil soğutma için mikro kanallı soğutma sisteminin uygulanabilirliği sayısal olarak araştırılmış ve mikro ölçekteki yüksek basınç düşüşleri nedeniyle normal ölçekli soğutma sistemi ile devam edilmesine karar verilmiştir. Bu nedenle, hava ve sıvı soğutmanın ayrı ayrı veya bütünleşik olarak uygulanabildiği bir hibrit soğutma sistemi geliştirilmiş ve pil modülüne uygulanmıştır. Pil modülü, üç adet lityum-iyon kese hücresinin seri bağlanmasıyla oluşturulmuştur. Deneyler sırasında ortam sıcaklığı 23ºC'de tutulmuş ve pil hücreleri 3C hızında deşarj edilmiştir. Sonuçlara göre, hava soğutma daha homojen bir sıcaklık dağılımı vermektedir. En düşük sıcaklık değerleri hibrit soğutma sisteminde gözlenmiştir ve hücreler arası sıcaklık farkı su soğutmalı sisteme göre %30 oranında azalmaktadır. Hava soğutmadaki sıcaklık profili, ortam sıcaklığındaki veya deşarj hızındaki olası bir artışın sonucu olarak optimum sıcaklık değerlerinin dışında kalınacağını göstermektedir. Hava soğutma sisteminin elektrikli araç aktif iken kapasitesini belirlemek adına pil modülü bir dizin sıra ile (3C-1C) deşarj edilmiştir. Sonuçlara bakıldığında, ortam sıcaklığı 23ºC iken, hava soğutma ile pil hücrelerin sıcaklığının 30ºC'nin altında tutulduğu görülmektedir. Hibrit soğutma sayesinde pil modülü için aracın kullanım durumuna göre uygun soğutma sistemini seçebilmekteyiz; dolayısıyla sistemin verimliliğini artırmaktayız.

Anahtar Kelimeler ve Deyimler: Batarya Modülü, Lityum-iyon Hücreler, Hibrit Soğutma

TABLE OF CONTENTS

LIST OF FIGURES

Figure **Page**

Figure **Page**

Figure **Page**

LIST OF TABLES

LIST OF SYMBOLS

Nomenclature

Be	Bejan number	-
Br	Brinkman number	-
C	Charge/discharge rate	-
C_p	Specific heat	kJ/kg.°C
CH	Measurements points on battery surface	-
d_h	Hydraulic diameter	m
D	Diameter	m
E_{oc}	equivalent circuit potential	V
F	Faraday's constant	C/mol
H	Height	m
i	Current density	A/m^2
i'	Discharge current per volume	A/m^3
Kn	Knudson number	-
L	Length	m
I	Current	A
M	Axial heat conduction number	-
n	Normal vector	-
N	Number of electrons	-
Nu	Nusselt number	-
P	Pressure	Pa
Pe	Peclet number	-
Po	Poiseuille number	-
Q	Heat generation	W
q	Volumetric heat generation	W/m^3
q'	Heat transfer per unit length	W/m
R	Resistance	ohm.m
Re	Reynolds number	-
S	Entropy	kJ/kg.°C
T	Temperature	°C

u, v, w	Velocity vectors in x, y and z directions	m/s
W	Width	m
V	Voltage	V

Abbreviations

AR	Aspect ratio	
BMS	Battery management system	
CC	Constant current	
CV	Constant voltage	
DC	Direct current	A
DOD	Depth of discharge	%
EDL	Electrical double layer	
HEX	Heat exchanger	
MCHS	Microchannel heat sink	
PCM	Phase change material	
SOC	State of charge	%

Greek Symbols

ξ	Zeta potential	V
ψ	Electrostatic potential	V
κ	Temperature jump parameter	
α	Thermal diffusivity	m^2/s
ϵ	Surface roughness	
ε	Roughness height	m
Δ	Change	
∇	Gradient	
$\emptyset$	Volume fraction of nanoparticle	%
γ	Convergence criterion	
ρ	Density	kg/m^3
μ	Viscosity	Kg/m.s
$\forall$	Volume	m^3
$\dot{\forall}$	Volume flow rate	m^3/s

Subscripts

cr	Critical
atm	Atmospheric
c	Channel
eff	Effective
f	Fluid
fin	Fin
i	Mesh index
in	Inlet
irr	Irreversible
oc	Open circuit
out	Outlet
rev	Reversible
s	Solid
sum	Summation
tab	Tab
wi	Inside wall
wo	Outside wall

CHAPTER 1

INTRODUCTION

1.1. Problem Statement

Research and development on electric vehicles are being focused in the worldwide due to concern about energy consumption and atmospheric air quality. In addition, recent developments in advanced rechargeable batteries for electric vehicles also contribute to adaptation of people to use electric vehicles. There are many kinds of rechargeable batteries and lithium-ion batteries have gained lots of interests as an energy storage solution for electric vehicles due to their high specific energy and power density compared to its competitors [Affanni et al. 2005; Pesaran et al. 2007, Chen et al., 2009, Mastali et al. 2016]. However, using batteries in electric vehicles brings new challenges such as thermal management, duration of charging, limit of range and so on. The temperature of a battery increases during charging/discharging and operation. The capacity, durability and safety of the lithium-ion batteries are highly affected by operating temperature [Bandhauer et al., 2011, Safari and Delacourt, 2011]. The durability and safety issues arise in the case of over-heating problem. In addition, the capacity of the battery decreases at low temperature [Horie et al. 2008]. Therefore, the temperature of a battery system should be kept in a certain range to prevents safety risks and maximizes capacity. Moreover, a thermal management system is necessary to achieve optimum performance from a battery system. There are various kinds of thermal management systems for batteries such as air cooling, liquid cooling, heat pipe cooling and so on [Li et al., 2019].

1.2. Aim and Objectives

The main aim of the study is to keep the battery cells in the optimal operating temperature range (15ºC ─ 35ºC) during charging, discharging and operation by documenting various cooling systems such as air, water and hybrid cooling. In the hybrid cooling system, air and water cooling imposed to battery cells solely or simultaneously in order to determine the cooling performance. The selected cooling system should be met the requirements of the battery system.

A battery module is manufactured by connecting three lithium-ion pouch cells in serial. A heat exchanger is designed and manufactured to obtain uniform temperature distribution along the battery module. The size of heat exchanger is kept as small as possible to minimize its weight and volume. Therefore, heat transfer and fluid flow characteristic in micro size heat exchangers are investigated. In addition, the feasibility of microchannels (comparison between heat transfer rate and pressure drop values) is investigated via a numerical study. According to the review and numerical study on microchannel heat sinks, it is decided to continue with a conventional heat exchanger in the cooling of battery cells because of higher pressure drop values in micro scales. Hence, the study is mainly experimental parts all of them are carried out at constant temperature (23 ºC) for battery module.

1.3. Limitations and Assumptions

The experiments are carried out in a large room which is not air-conditioned. Therefore, there were several degrees Celsius temperature fluctuations during experiments which are considered to be approximately constant. All the temperature and voltage values are measured by thermocouples.

The temperature of battery cells in a battery module is measured by thermocouples which are located near the positive tab. As we know from the literature, the temperature is not constant through the battery surface and it is dense near the tabs. Therefore, the highest temperature values on the battery surfaces are considered during the study.

There are some limitations related to cable connections. The connection of battery cells and charging/discharging devices are very important to get more accurate results. If the connection of battery is not made properly, it is possible to observe unexpected temperature rise and uneven temperature differences between the cells.

Manufacturing of the heat exchanger is limited by the available sources. Actually, it is not possible to reach desired dimensions for the materials from the market, such as copper tubes, plates and etc.

1.4. Thesis Outline

The thesis consists of eight chapters. The second chapter is mainly based on literature studies about the electric vehicle batteries, thermal management of battery systems and microchannel heat sinks concept.

In chapter three, a numerical study on the heat transfer enhancement in microchannel heat sink is conducted. COMSOL Multiphysics, v5.0 (COMSOL, 2014), is selected as computational software in the numerical analysis of heat transfer and fluid flow.

In chapter four, the methodology of the thesis is given. The thesis is mainly consisting of experimental studies. Hence, measurement methods, utilized devices and charge/discharge procedures are presented in the chapter. Also, accuracy of devices is given in the chapter. The general concepts for the experimental procedure and measurement methods are introduced.

The chapter five contains different approaches used in the study of battery systems. One of the approaches is using silicone heater system as a solution for the battery studies. A silicone heater system is utilized in the experimental setup to reflects the thermal behaviour of a real battery. In the second part, an experimental study is conducted on a single battery cell. The temperature distribution on the battery surface is measured via thermocouples and monitored by using a thermal camera.

Chapter six is the main part of the thesis. In the chapter, the experimental setup for a battery module which is created by connecting three lithium-ion pouch cells in serial, is represented.

In the chapter seven, the results of the experimental studies which are based on battery module are introduced. Various cooling methods introduced to the battery module and main outcomes are figure out via graphs. The last chapter is based on evaluation of the results.

CHAPTER 2

LITERATURE REVIEW

Thermal management of battery cells is an important concept for electric vehicles. The performance of the battery cell is highly affected by operating temperature and safety issues arise in electric vehicles because of overheating. Therefore, a cooling system is a necessity for battery cells to increase performance and eliminate safety problems. The temperature and heat generation profiles in battery cells should be covered before introducing a cooling method. Therefore, the literature part is divided into three sections and starts with the description of battery system. Firstly, the battery system is defined by their mechanical, chemical and thermal properties. Furthermore, thermal behaviour of battery cells (temperature distribution and heat generation profiles) is also investigated in detail. In the second part of the literature chapter, thermal management systems used in the battery systems are studied. Finally, heat transfer and fluid flow characteristics in microchannel heat sinks (MCHS), which is aimed to introduce as a cooling system for battery cells, are reviewed in detail.

2.1. Description of Battery Systems

One of the essential components in the electric vehicle is battery cell (Wang, 2006). There are many battery types used in electric vehicles and lithium-ion batteries have gained much interest among them since they have high power density to volume ratio (Affanni et al., 2005, Pesaran et al., 2007, Chen et al., 2009, Mastali et al., 2016; Mukane et al., 2021). The lithium-ion batteries have been fabricated in various shapes and configurations such as cylindrical, coin, prismatic(rectangular), pouch and thin-flat. The study is conducted for the pouch cell geometry in the thesis.

A lithium-ion unit cell consists of a negative electrode, a separator and a positive electrode which are sandwiched between two current collectors. Schematic representation

of a unit cell and a battery cell are given in Figure 2.1 (Smith and Wang 2006; Hosseinzadeh et al., 2017). Aluminium and copper are commonly used metals for positive and negative current collectors, respectively.

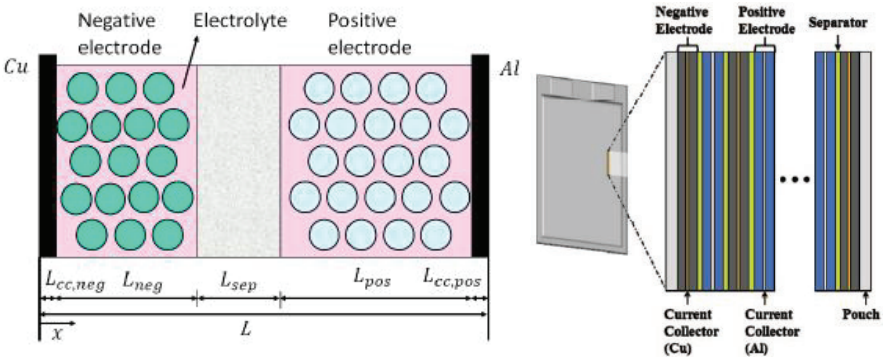

(a) (b)

Figure 2.1. Schematic representation of a unit cell and a battery cell

(Source: Hosseinzadeh et al., 2017; Smith and Wang, 2006)

The capacity and performance of the electric vehicle mainly depend on battery cell. In addition, most of the safety problems in electric vehicles are because of battery systems (Horie et al., 2008; Bandhauer et al., 2011; Safari and Delacourt, 2011). The battery system hierarchy in an electric vehicle is shown in Figure 2.2 (Al-Hallaj and Selman, 2002). A battery module contains many battery cells and a battery pack is created by connecting many battery units (hundreds and thousands) in serial or parallel configuration. The number of battery cells and battery modules in a battery pack is defined with respect to desired battery voltage and capacity (Karimi and Li, 2013).

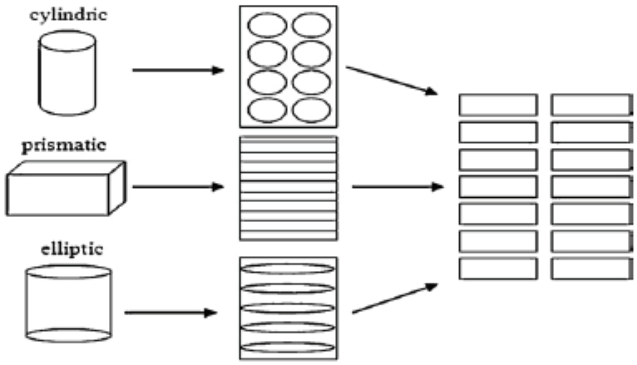

Figure 2.2. Configuration of the battery system; battery cell, battery module and battery pack (Source: Al-Hallaj and Selman, 2002)

2.1.1. Heat Generation in a Battery Cell: Mathematical Formulation

In a battery cell, heat is generated by (i) entropy change due to electrochemical reactions and (ii) Joule's effect (ohmic heating) caused by current transfer across internal resistances (Karimi ve Li, 2013). The heat generation rate in a battery cell can be calculated by using Equation (2.1) (Bernardi et al., 1984; Chen and Evans, 1994):

$$Q = Q_{irr} + Q_{rev} = I(E_{oc} - V) - IT\frac{dE_{oc}}{dT} \tag{2.1}$$

where q is heat generation rate, I is current ($I > 0$ for discharge, and $I < 0$ for charge), E_{oc} is equilibrium cell voltage (also called as open circuit voltage), V is cell voltage, T is temperature of the cell and dE_{oc}/dT is the temperature coefficient. The first term, $I(E_{oc} - V)$, is heat generation resulting from ohmic and other internal resistances present in the cell (also called as irreversible heat generation or Joule's heating) and the second term, $-IT\,[dE_{oc}/dT]$, is heat generated or consumed because of the reversible entropy change, resulting from cell electrochemical reactions. Reversible heat generation in a battery cell is related to entropy change and it is also represented by Equation (2.2) (Karimi and Li, 2013).

$$Q_{rev} = -i'T\frac{\Delta S}{NF} \tag{2.2}$$

where i', ΔS, N and F represents the discharge current per unit volume, entropy change, number of electrons in the reaction and Faraday's constant (96485 C/mol), respectively.

Beside heat generation rate in a battery cell which is calculated by Equation (2.1), heat generated in the current collecting tabs is also considered in the study of Yi et al. (2013) and it is defined as:

$$Q_{tab} = (R + R_c)i^2 \tag{2.3}$$

where R and R_c represent resistivity of the current collecting tab and electrical contact resistance between the current collecting tab and the lead wire connecting the battery cell. i is defined as the current density with respect to the cross-sectional area of the current collecting tab.

All the equations, are used in the calculation of heat generation rate in batteries, are investigated and total heat generation in a battery cell is indicated by Equation (2.4) [Xiao and Choe, 2013].

$$Q_{sum} = Q_{irr} + Q_{rev} + Q_{tab} \tag{2.4}$$

The calculation of total heat generation in a battery cell is possible via Equations (2.1) - (2.4), but some of the terms are change over time (i.e., $\frac{dE_{oc}}{dT}$), so in the calculation of time dependent variables, experimental values from the literature studies should be taken into consideration. Therefore, in order to conduct a study without using real batteries, researchers should be followed these ways: (i) utilized a software which

contains a solution approach for battery systems, or (ii) use experimental results for time dependent parameters which are presented in the literature.

2.1.2. Thermal Behaviour of Pouch Cells During Charging, Discharging and Operation (Heat Generation and Temperature Distribution Profiles)

Heat generation in a battery is change with respect to battery type, capacity, charge/discharge condition and environmental temperature. These are the general parameters that affects the heat generation behaviour of the batteries. In addition to these parameters, chemical reaction inside the cell also affects the heat generation characteristics of the battery cell.

Numerous investigations have been made on the heat generation and temperature distribution along the battery surface. Heat generation is dense near connection points (tabs or busbars) with respect to literature. There are two main reasons for why high temperature values are observed near tabs/busbars. The first one is that ionic distribution between the positive and negative tabs. This situation is documented in the study of Li et al. (2019). In Figure 2.3, the movement of ions from negative tab to positive tab during discharge is shown clearly. More ions move in the upper part of the pouch cell and current density is high at that part.

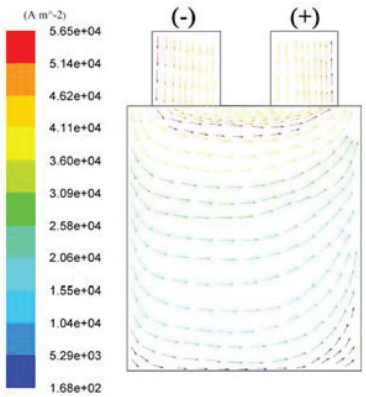

Figure 2.3. Ionic distribution between the positive and negative tabs at 1C discharge (Source: Li et al., 2019)

The second one is that heat generation in the current collecting tabs. As mentioned in the Chapter 2.1.1, there is a heat generation in the tabs, and it flows through the battery surface. As the contribution of these two parameters, heat generation in battery cells becomes dense near the tabs and decreases through the other sides of the battery cells. The change of volumetric heat generation values along the surface of pouch cell is shown in Figure 2.4.

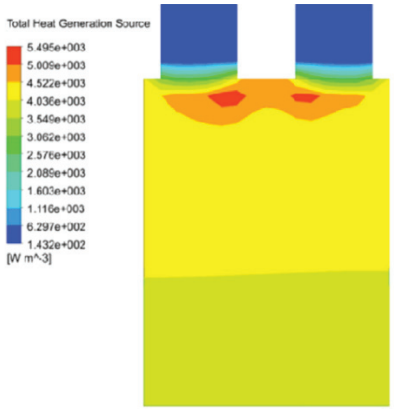

Figure 2.4. Heat generation distribution along the battery surface at 1C discharge rate (Source: Li et al., 2019)

The heat generation inside the battery cell increases with the battery capacity (Arora and Kapoor, 2019). The change of heat generation rate with respect to depth of discharge (DOD) for battery cells with different capacities is shown in Figure 2.5. The batteries discharging at 3C rates when ambient temperature is 20ºC. According to the Figure 2.5, heat generation rate increases with increasing depth of discharge. There is a remarkable difference in the heat generation rates of different capacity cells at the end of the discharge. The difference between the heat generation rates become significant at high capacities.

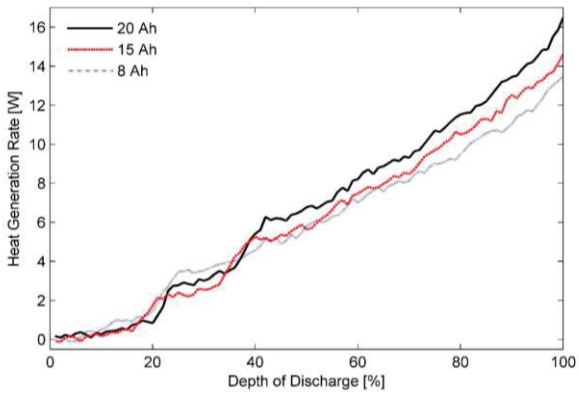

Figure 2.5. The change in heat generation during 3C discharging for different capacity batteries (20 ºC) (Source: Arora and Kapoor, 2019)

One of the other parameters which affects the heat generation behaviour of a battery cell is the environmental temperature. This effect can be explained by the change of battery internal resistances via environmental temperature. At low temperatures, the internal resistance of battery cell rises and electrical current decreases. As a result, the amount of heat generated in the battery cell increases. In the literature, it is pronounced that heat generation in a battery cell is inversely proportional to environmental temperature (Chen et al., 2014; Arora et al., 2017; Lin et al., 2018). This situation is represented in Figure 2.6 (Lin et al., 2018). According to Figure 2.6, the high amount of heat is produced at low ambient temperatures. The difference between the heat generation rates is significant at the beginning of the discharging.

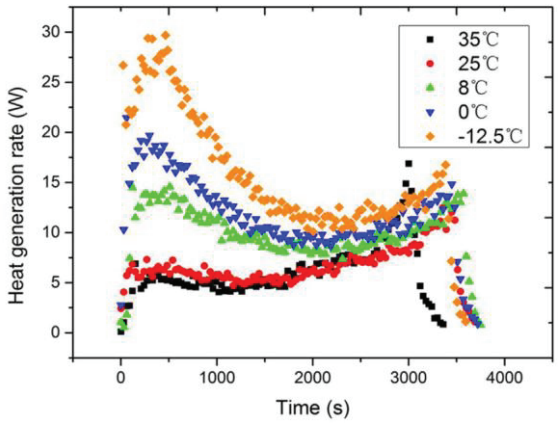

Figure 2.6. The change of heat generation at various environmental temperature with respect to time at 1C rate discharging (Source: Lin et al., 2018)

The last parameters of that section which affects the heat generation rate of a battery cell is charge/discharge rate. The duration of charging/discharging is defined by "C" rate. 1C rate means that charge/ discharge of a battery will be completed in one hour. Similarly, charging/discharging of a battery cell will be completed in 2 hours and 30 minutes for 0.5C and 2C rate, respectively. Therefore, C rate is inversely proportional with time and huge amount of heat releases in a short time interval at high C rate. In the literature, it is documented that heat generation in a battery increases with C rate (Chen et al. 2014; Bazinski and Wang, 2016; Lin et al., 2018). The increment in the heat transfer rate with respect to the C rate shows an exponential trend as it is indicated by Figure 2.7 (Lin et al. 2018).

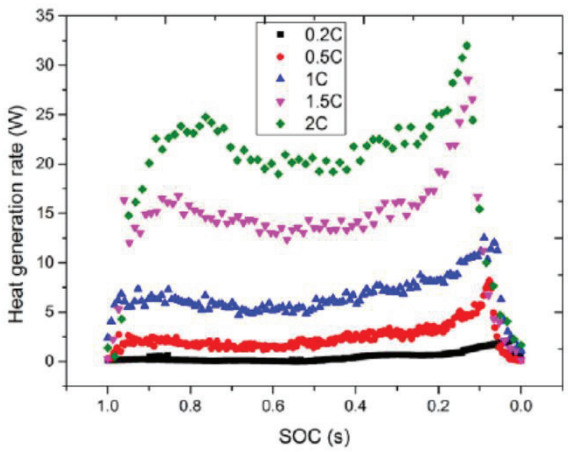

Figure 2.7. The change of heat generation during discharging at different C rate when the temperature is constant (Source: Lin et al., 2018)

Xie et al. (2018) experimentally and numerically investigated heat generation characteristic of a lithium-ion battery cell under different temperature and discharge/charge rates. They stated that maximum heat generation occurs at the highest discharge rate. Also, they indicate that the charging/discharging time become longer with the rise in ambient temperature.

The effect of various parameters like capacity, ambient temperature, and etc., on the generation rate in a battery cell are discussed above. In addition to these parameters, the contribution of connection points, which occurs between battery tabs in a battery module, to total heat generation rate should be considered. The effect arises in module

and pack level in the battery system. In the study of Keyser et al. (2017), this situation is explained by 22% increment in the heat generation rate per cell when the cell placed inside the battery pack instead of operating single cell. The main reason behind this increment is heat generation in the connection points. The difference in heat generation between a single cell and a cell in a battery pack with respect to the discharge rate is shown in Figure 2.8. As it shown in Figure 2.8, the difference between heat generation rates of a single cell and a cell in a battery pack increases with the discharge rate and it takes its largest value (33%) at the end of the discharge.

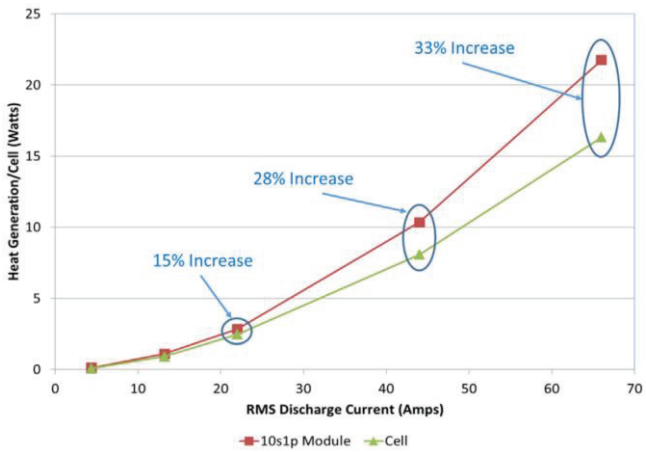

Figure 2.8. The change in the total heat generation for a single cell and a cell in the battery module with respect to discharge current (Source: Keyser et al., 2017)

In addition to the parameters mentioned above, there are some conditions which affect the temperature distribution on a battery surface. One of the conditions is tab configuration. Kim et al. (2008) experimentally and numerically studied the effect of electrode configuration on the thermal behaviour of a battery system. Their experimental results show that the highest temperature values are observed around the tabs. Figure 2.9 shows the temperature distribution along a battery cell during discharge for different electrode configurations. As it shown in Figure 2.9 (a-b), the heat generation is dense around positive terminal tab and the temperature distribution along the battery surface is changed by tab configuration.

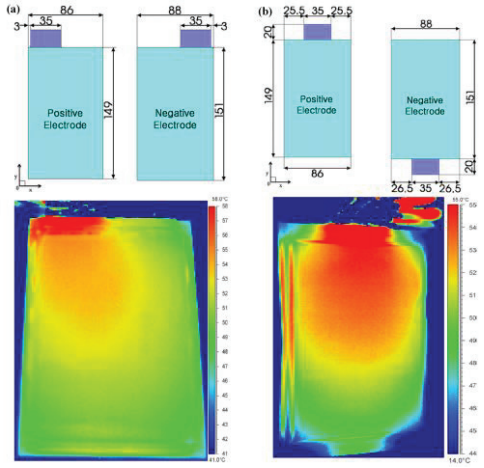

Figure 2.9. Temperature distribution along a battery cell surface during discharge for different tab configuration (Source: Kim et al. 2008)

The change of temperature distribution on the surface of a battery cell over time is covered experimentally and numerically by Goutam et al. (2017). They stated that maximum heat generation occurs around the positive tab core during the discharge. However, at the end of the discharge, maximum temperature values are recorded at the upper part of the pouch cell. As can be seen from Figure 2.10, the temperature difference along the cell is almost 5ºC.

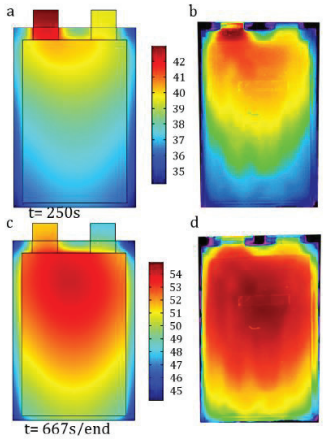

Figure 2.10. Temperature distribution along a battery cell during the discharge and at end of the discharge: numerical and experimental results (Source: Goutam et al, 2017)

Literature demonstrates that heat generation and temperature distribution in a battery cell are not uniformly distributed along the cell surface during charging, discharging and operation. The heat generation is dense around the tabs of the battery cell. Also, there are many parameters which effect the heat generation rate in a battery cell and temperature distribution on the battery surface such as capacity, ambient temperature, charge/discharge rate, tab configuration and etc.

2.2. Thermal Management Systems for Batteries

Thermal management system is crucial in order to increase performance of the battery cell and eliminating safety issues (preventing overheating and thermal runaway) by controlling operating temperature values (Maleki et al. 1999; Xun et al., 2013; Fathabadi, 2014; Vertiz et al. 2014; Mastali et al., 2018). There is an optimum temperature range (0°C ─ 65°C) for battery cells in order to keep lifespan, capacity and performance as high as possible (Karimi ve Li, 2013). Actually, optimum temperature range is change with respect to the battery type, for instance, lithium-ion batteries provide the best performance at temperatures between 25°C ─ 40°C (Pesaran, 2002; Dan et al., 2019). The optimum operating temperatures can be changed with respect to battery type, however, 25°C ─ 40°C is treated as ideal environmental conditions for most of the batteries (Yeow et al., 2012; Pesaran, 2002). The lifetime, capacity and performance of the battery cells highly effected by operating temperatures. At the low temperatures, (<15ºC), the ionic distribution is become slow and the performance of the battery decreases (Zhang et al., 2017). At high temperatures, (>35ºC), chemical reactions inside the battery occur very fast. This situation inversely affects the lifetime of the battery (Xu et al., 2017). Beside these factors, there is an additional parameter effecting the performance of the battery cell: temperature difference. The temperature differences among the cells in a battery pack highly affects cell performances and, aging problems arise due to high cell-to-cell temperature difference (Saw et al., 2016; Han et al., 2019; Feng et al., 2019). The temperature difference along the battery surface should be less than 5ºC (Chung and Kim, 2019). Thermal runaway can be occurred in battery packs at the high temperature values and under large temperature differences, and it has resulted in fire of the cells. This situation shows the necessity of the cooling system for battery

cells. Also, the capacity of the cooling system should be defined with respect to the capacity of the battery system.

There are two main approaches in thermal management of lithium-ion batteries: decreasing heat generation rate inside the battery cell and increasing the heat dissipation rate outside the battery. In the first approach, the electrochemical performance of the cell is improved by reducing the thermal resistance of the battery. In the second approach, the heat transfer rate from the battery surface to environment is improved in order to reduce temperature in the battery. Also, distributing heat uniformly through the battery surface is one of the objectives of the second approach (Mastali et al., 2018). Different types of cooling systems have been developed for the second approach such as air cooling (Fathabadi et al. 2014), liquid cooling (Tong et al. 2015), heat pipe cooling (Zhao et al. 2015) and phase-change material cooling (Lin et al. 2015). Also, application methods of the cooling systems are separated into two categories: direct cooling and indirect cooling. In the direct cooling, there is a direct contact between the heat transfer surfaces of battery cell and coolant medium. However, in the indirect cooling an extra equipment placed between the coolant medium and the heat transfer surfaces of battery cell to transfer heat from one medium to other medium. Figure 2.11 shows schematically the direct and indirect cooling systems used in the study of Teng and Yeow (2012). They are numerically covered the application of direct and indirect cooling systems on a pouch cell battery. They stated that direct liquid cooling is more efficient than indirect liquid cooling at the same flow rate of coolant.

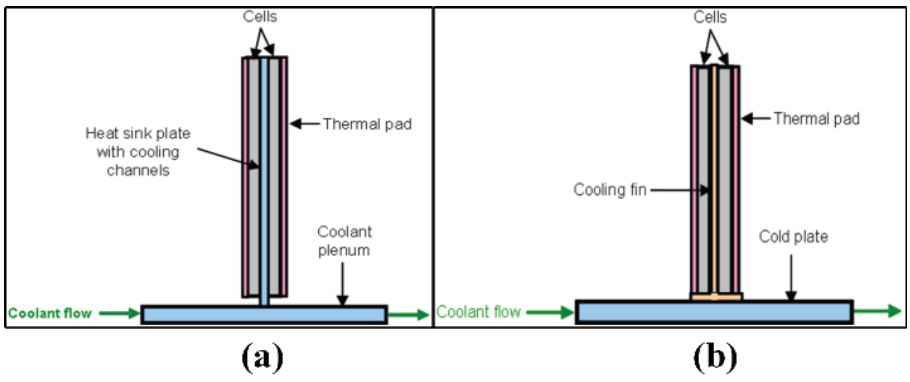

Figure 2.11. Illustration of (a) direct and (b) indirect liquid cooling
[Source: Teng and Yeow, 2012]

The limitations and merits change with respect to the cooling methods. Air cooling is the simplest approach among the cooling methods and more uniform temperature distribution can be obtained in the system. However, the capacity of the air cooling is limited. The temperature rise in the battery can mitigate via forced-air cooling, but during aggressive driving circles and at high operating temperatures it will inadequate and will cause a large nonuniform temperature distribution (Zhao et al., 2015; Lin et al., 2015). In the literature, it is stated that air cooling can be affective when the heat generation per cell is smaller than 10 W (Teng and Yeow, 2012). In the high-capacity battery cells and at high charge/discharge rates, liquid cooling is a feasible solution for the cooling of battery cells. The main drawbacks in the liquid cooling systems are complexity, cost and potential leakage. Adding phase change materials will cause extra weight and will be occupied extra volume in the battery pack. Also, heat absorbed from phase change materials during continuous cycling also need to exhaust from the system. The main limits in the beat pipe cooling systems are gravity, weight and passive control system (Chen et al. 2016).

Chen et al. (2016) numerically surveyed the cooling methods for a pouch cell geometry. They investigated four types of cooling: air cooling, fin cooling and liquid cooling (direct and indirect). The configuration of the cooling systems is given in the Figure 2.12. The results figure out that maximum temperature difference along the surface of the battery cell was obtained in indirect liquid cooling because of the longest cooling channels.

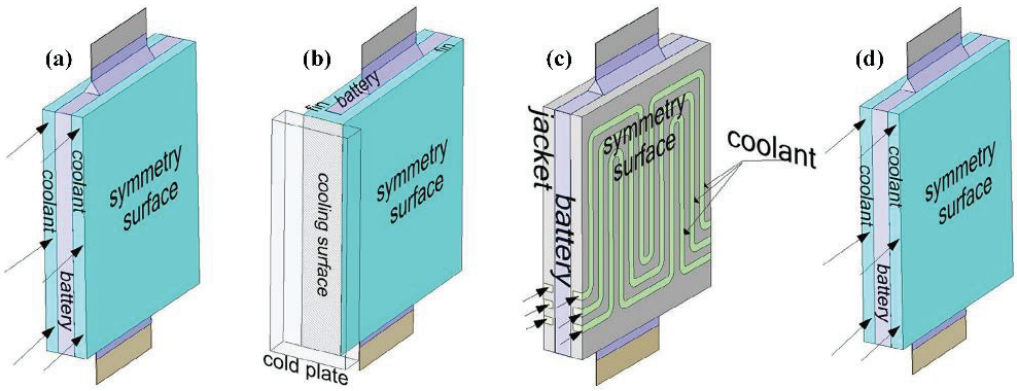

Figure 2.12. Different cooling methods and their configurations; (a) air cooling, (b) fins cooling, (c) indirect liquid cooling and (d) direct liquid cooling (Source: Chen et al. 2016)

2.2.1. Air Cooling

Air is commonly used in the cooling of electric vehicles because of simple equipment requirements and reliable system operations. Cooling of the battery cell is easily achieved by supplying air directly through the battery module. However, air cooling is not suitable for the cooling of battery module in the extreme conditions, such as at high charge/discharge rate (Wang et al. 2015).

Air-based cooling can be divided into two main categories: natural convection and forced convection. There are some variations in the application of air cooling system such as air flow velocities, flow path and geometrical arrangement of the batteries in the pack (Al-Zareer et al., 2018).

Fathabadi et al. (2014) numerically tested the cooling of a battery system in case of natural convection. The application method of air cooling to the battery unit is shown in Figure 2.13. They state that battery have been cooled effectively by air cooling at various environmental conditions (up to 48°C). They also stated that at high environmental temperatures (>48°C), forced convection need to be applied to the system in order to cool battery units effectively.

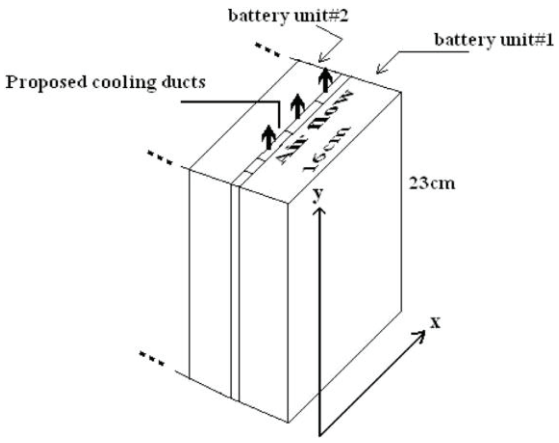

Figure 2.13. Battery pack design with the proposed cooling media
(Source: Fathabadi et al. 2014)

2.2.2. Liquid Cooling

There are various application methods for the liquid cooling in a battery module. The heat transfer by liquid cooling can be accomplished by through discrete tubing around each battery module, with a jacket around the battery module, submerging battery modules in a dielectric fluid for direct contact or placing the battery module on a liquid cooled plate (heat sink concept) (Wang et al., 2015). Liquid cooling is more complicated than air cooling, but it is more effective than air cooling under aggressive cycling.

Huo et al. (2015) numerically documented cooling of a battery cell by utilizing cold plates with various number of cooling channels. The effect of number of channels, flow direction, mass flow rate and ambient temperature on the temperature rise and temperature distribution in a battery during the discharge are evaluated with a comprehensive numerical study. The results show that the maximum temperature values in the battery cell is decreases when the number of cooling channels increases. In addition, based on the 6 channels liquid cooling system, they numerically surveyed the effect of flow direction on the temperature distribution and the results are represented by Figure 2.14. According to the results, the lowest temperature values are observed in Design 1 and Design 5. Also, Design 1 gives the most uniform temperature distribution for cold plate when compared to other designs. Thus, the authors decide to continue their research on Design 1 by considering the cost, complexity of other designs.

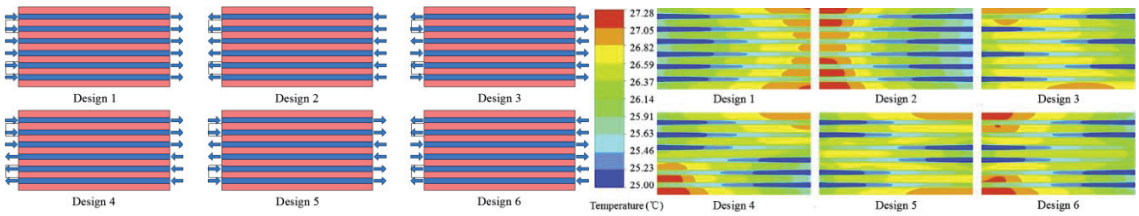

(a) (b)

Figure 2.14. Schematics of (a) different flow directions and (b) corresponding temperature distribution at the end of the discharge (Source: Huo et al. 2015)

2.2.3. Phase Change Material (PCM) Cooling

Phase change materials (PCM) is firstly introduced by Hallaj and Selman (2002) as a possible solution for the cooling of battery systems and it takes more attention in recent years. The main working principle of PCM cooling is that the heat generated by battery cell during discharge is stored as latent heat in the PCM and is transferred to the cell module during relaxation to keep its temperature constant (Wang et al., 2015). The main advantages of PCM are low maintenance cost and providing temperature uniformity. The main drawbacks in the PCM cooling are that it is caused extra weight and the cooling capacity is limited under aggressive driving circles.

2.3. Heat Transfer in Microchannels

There are various types of cooling methods used in electric vehicles such as air cooling, heat pipe cooling, PCM cooling and so on. In addition to these methods, microchannel heat sinks (MCHS) can be used as an alternative solution for the thermal management of a battery cell. MCHS are capable of enhancing heat transfer rate due to their high surface to volume ratio relative to the conventional heat sinks (Tuckerman and Pease, 1981; Guo and Li, 2003; Kumaraguruparan and Sornakumar 2010; Kandlikar, 2012; Yadav et al., 2016, Vajdi et al., 2020). However, increase in the heat transfer surface area yields the penalty of increased pressure drop. (Tuckerman and Pease, 1981; Guo and Li, 2003; Garimella and Singhal, 2004; Kandlikar et al., 2006; Xie et al., 2009; Dang and Teng, 2011; Dewan and Srivastava, 2015; Vajdi et al., 2020; Coşkun and Çetkin, 2020) The feasibility of MCHS can be uncovered by finding maximized heat transfer rate for acceptable pressure drop values. Hence, this part will be based on literature survey about heat transfer in microchannels and summary of the studies which are mainly based on heat transfer and fluid flow characteristic in MCHS. In addition, studies which are used MCHS in the cooling of electric vehicles will be documented in the last part of that section.

Heat transfer channels can be classified with respect to their hydraulic diameter as macro, mini, micro, and nano channels. Microchannel heat sink concept was firstly introduced by Tuckerman and Pease (1981). They stated that a channel can classify as microchannel if the hydraulic diameter ranges from 0.01 mm to 0.2 mm. Table 2.1 shows the classification of heat exchanger based on their channel sizes (Mehendale et al., 2000; Kandlikar and Grande 2002). The channels can be classified as microchannel if the hydraulic diameter lied in between 0.001-1 mm (Gad-el-Hak 1999; Morini, 2004). Microchannel heat sinks (MCHS) are capable of enhancing heat transfer rate due to their high surface to volume ratio relative to the conventional heat sinks (Tuckerman and Pease, 1981; Guo and Li, 2003; Kumaraguruparan and Sornakumar 2010; Kandlikar, 2012; Yadav et al., 2016).

Table 2.1. Classification of heat exchangers with respect to hydraulic diameter

Mehendale et al. 2000		Kandlikar and Grande 2002	
Micro HEX	$1\mu m < d_h \leq 100\mu m$	Transitional channel	$0.1\mu m < d_h \leq 10\mu m$
Macro HEX	$100\mu m < d_h \leq 1mm$	Microchannel	$10\mu m < d_h \leq 200\mu m$
Compact HEX	$1mm < d_h \leq 6mm$	Mini channel	$200\mu m < d_h \leq 3mm$
Conventional HEX	$6mm < d_h$	Conventional channel	$3mm < d_h$

Microchannel heat exchangers have been utilized in numerous fields of engineering applications such as electronics, automotive industry, fuel cells, air conditioning systems, and some of them are shown in Figure 2.15.

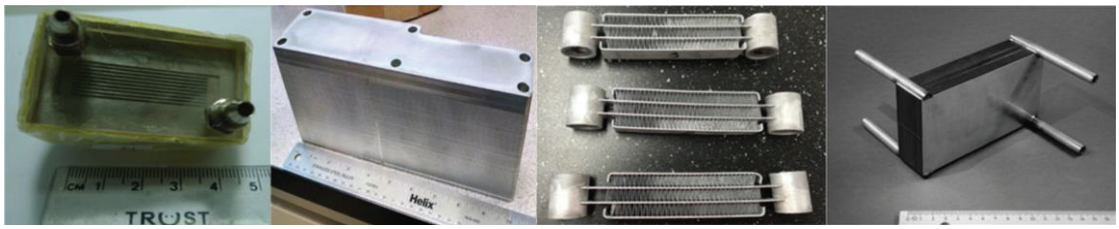

(a) (b) (c) (d)

Figure 2.15. Microchannel HEXs utilized in (a) electronic cooling (b) natural gas cooling in automotive industry (c) air conditioning (d) fuel cells (Source: Dang and Teng, 2011; Knight et al., 1992; Zhao et al., 2016; Lee et al., 2002)

In micro sizes, majority of the cases are laminar because of relatively small hydraulic diameters compared to conventional sizes. Generally, transition from laminar to turbulent flow is occurred earlier than in conventional length scales ($Re_{cr} = 2300$) (Guo and Li, 2003; Yuan et al., 2016; Peng and Peterson, 1995). Some of the obtained critical Reynolds number values for MCHS are given in Table 2.2.

Table 2.2. Transition from laminar to turbulent flow for MCHS

Study	Critical Reynolds Number
Wu and Little (1983)	400-900
Peng and Peterson (1995)	1000
Harms et al. (1999)	1500
Yuan et al. (2016)	1500
Li et al. (2003)	1700

MCHS studies in the literature are categorized with respect to heat transfer mechanisms, fluid flow characteristic and solution methods. The schematic representation of how the studies can be categorized is shown in Figure 2.16.

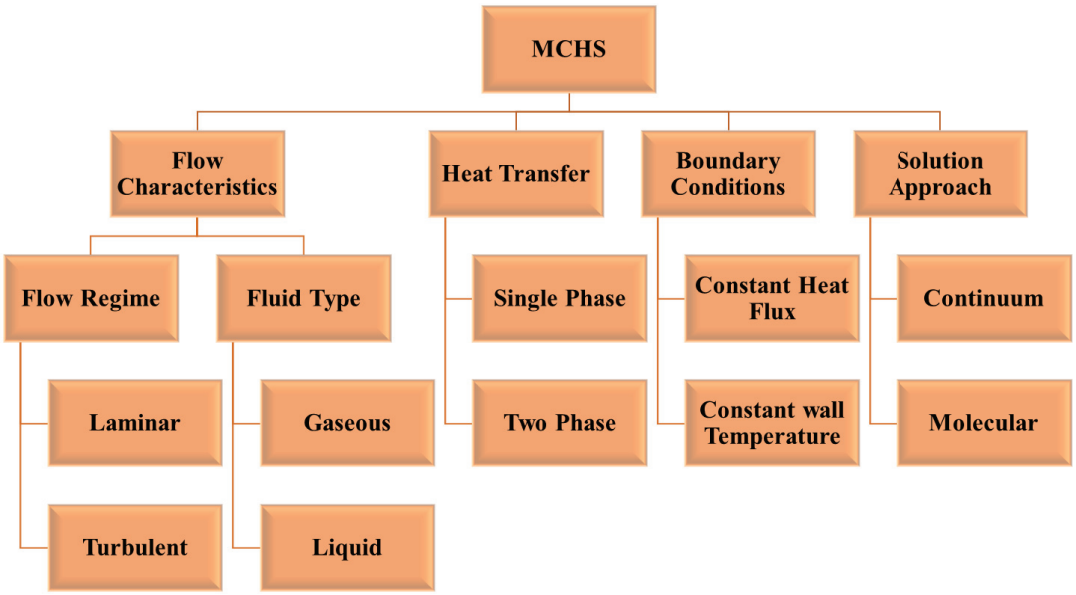

Figure 2.16. Schematic representation of MCHS categorization

2.3.1. Scaling Effects in MCHS

In continuum approach (macro scale) some physical phenomena can be ignored while evaluating heat transfer and pressure drop characteristics (surface roughness, EDL effect, viscous dissipation, rarefaction, aspect ratio, axial heat conduction). However, as the length scale decreases, the effect of these physical phenomena become essential, and; therefore, they needed to be considered in order to evaluate heat transfer and flow characteristic accurately. Validity of continuum approach in micro scale needed to be carefully investigated, especially for gaseous flow (Kandlikar et al., 2006). Knudsen number (Kn), (free molecular path/characteristic flow dimension), is utilized to characterize the flow regime of gaseous flow in MCHS and the flow is treated in continuum medium if Kn number is smaller than 0.001. Continuum assumption cannot be used as Kn number becomes greater than 0.001 and rarefaction effect becomes significant on heat transfer for gaseous flow (Kakaç et al., 2005; Sen and Darici, 2017). Flow regimes with respect to Kn number are listed in Table 2.3 (Kandlikar et al., 2006; Arkilic et al., 1997; Jayaraj et al., 2007). In slip flow regime, the temperature and velocity profiles differ from continuum regime and the differences explained by slip velocity and temperature jump (Sen and Darici, 2017). This situation indicates that there is no thermodynamic equilibrium between the fluid particles and channel wall surfaces at the boundary of the channel walls in the presence of slip velocity and temperature jump (Kalyoncu and Barisik, 2016).

Table 2.3. Flow regimes for gaseous flow at various Kn number values
(Source: Kandlikar et al., 2006; Arkilic et al., 1997; Jayaraj et al., 2007)

Knudsen number	Flow regime	Solution Method
$Kn \rightarrow 0$	Continuum (no molecular diffusion)	Euler equations with slip-BCS
$Kn \leq 0.001$	Continuum (with molecular diffusion)	NS equations with no-slip-BCs
$0.001 < Kn \leq 0.1$	Slip flow (slightly rarefied)	NS equations with slip-BCs
$0.1 < Kn \leq 10$	Transient flow (moderately rarefied)	Burnett equations with slip-BCs Moment equations Lattice Boltzmann Direct simulation Monte Carlo
$Kn > 10$	Free molecular flow	Collisionless Boltzmann Direct simulation Monte Carlo

2.3.1.1. Surface Roughness

Relative surface roughness can be defined as the ratio between the roughness of the surface material (ϵ) and hydraulic diameter (d_h) of a microchannel. In macro scale (conventional) channels, importance of surface roughness pronounced only in turbulent regime (Xu et al., 2000; Sahar et al., 2016). However, it is essential for microchannels even in laminar region (Rosa et al., 2009); although it is a debated topic in the literature (Guo and Li, 2003; Peng et al., 1995; Weilin et al., 2000; Zhou and Yao, 2011; Sahar et al., 2016; Steinke and Kandlikar, 2006). Surface roughness along the microchannel (Sun and Faghri, 2003) is schematically shown in Figure 2.17. ε is the roughness height, and the effect of surface roughness increases as the height increases.

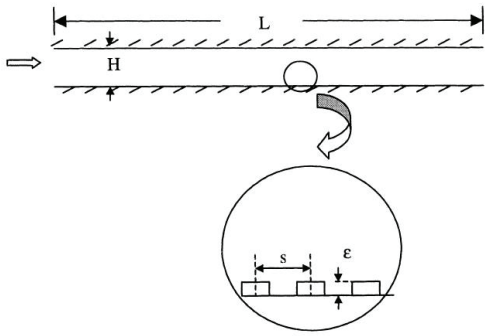

Figure 2.17. Schematic representation of the surface roughness in the microchannel (Source: Sun and Faghri, 2003)

Steinke and Kandlikar (2006) stated that researchers should consider surface roughness effect in their studies. Most of the studies state that Nusselt number (Guo and Li, 2003; Yuan et al., 2016; Wu and Cheng, 2003; Liu et al., 2015) and friction factor (Guo and Li, 2003; Weilin et al., 2000; Wu and Cheng, 2003; Liu et al., 2015) increase as surface roughness increases. Guo and Li (2003) states that early transition from laminar to turbulent flow in MCHS is due to surface roughness. Some researchers (Guo and Li 2003; Weilin et al., 2000; Rahman, 2000) also state that the distinction in between experimental and theoretical values are due to surface roughness. Liu et al. (2015) stated that the effect of surface roughness cannot be neglected when Reynolds number is greater

than 1500. In addition, Dai et al. (2014) stated that the roughness effect on friction factor and critical Re number need to be considered at high the relative surface roughness values (>1%). Moreover, researchers state that at low Kn number values (<0.02), the effect of surface roughness on friction factor becomes greater (Kleinstreuer and Koo, 2004). Kandlikar et al. (2003) experimentally investigated the effect of surface roughness on friction factor and heat transfer rate using two pipes with different inner diameters: 0.62 and 1.067 mm. They document that for 1.067 mm pipe diameter, the effect of surface roughness on heat transfer and pressure drop is insignificant when compared to 0.62 mm pipe diameter. Zhang et al. (2019) stated that Nu number and Po number in rough microchannels are not only related to shape of cross section of the channel but also related to the Re number of liquid flows. However, Croce and D'Agaro (2005) indicated that the effect of surface roughness on heat transfer is insignificant (within experimental error limits) and it highly depends on tube geometry. In addition to that, some of the researchers stated that overall thermal performance of a HEX does not change with surface roughness (Liu et al., 2015; Yuan et al., 2016). Furthermore, Pelevic and Meer (2016) indicated that surface roughness has minor effect (only 4% increase in heat transfer for 2.93% relative roughness) on heat transfer enhancement in their numerical study.

2.3.1.2. Electrical Double Layer (EDL)

EDL is related to electrostatic surface charge on the heat transfer surfaces, and it is formed on the heat transfer wall surfaces as reformation of charges on the solid surface and balancing charges in the liquid. It affects heat transfer and fluid flow due to interaction between the solid surfaces and aqueous solution (Kandlikar et al, 2006; Mala et al., 1997). EDL effect is essential for flow of liquids in microchannels (Mala et al., 1997; Ng and Tan, 2004; Tan and Ng, 2006). Schematic representation of the EDL at the channel wall 80 is shown in Figure 2.18. ξ and ψ are electric potential at the boundary between the diffuse double layer and the compact layer (zeta potential) and electrostatic potential at any point in the electric double layer, respectively.

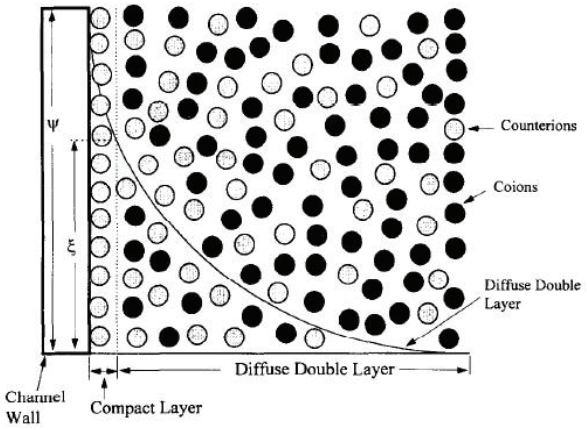

Figure 2.18. Schematic view of the EDL at the channel wall
(Source: Hunter, 1981; Mala and Li, 1999)

Ng and Tan (2004) stated that EDL effect decreases the effectiveness (actual heat transfer rate over maximum possible heat transfer rate) of the microchannel. They define EDL effect as a body force in the z-direction momentum equation (Ng and Poh, 2001; Tan and Ng, 2006). Ren et al. (2001) and Li (2001) showed that EDL effect increases pressure drop in microchannels. Mala et al. (1997) states that heat transfer rate in microchannels decreases because of EDL effect, and it is dominant at the vicinity of walls. The literature documents that friction factor increase (Mala et al., 1997; Yang et al., 1998, Yang and Li, 1998) and Nu number decrease due to EDL (Mala et al., 1997; Yang et al., 1998). The mean increment in the friction factor and decrement in Nu number was recorded as 17% and 8%, respectively in the study of Yang et al. (1998) for 200 mV zeta potentials and 10^{-8} M ionic concentration.

2.3.1.3. Axial Heat Conduction

Maranzana et al. (2004) numerically and theoretically studied the effect of axial heat conduction on heat transfer of MCHS. They stated that efficiency of heat exchanger is reduced in the presence of axial heat conduction. They point out that axial heat conduction is the reason why numerical and theoretical results do not match. They suggested that axial heat conduction needed to be defined during the numerical solution

phase in order to overcome the mismatch. In addition, they defined a new dimensionless quantity, M axial heat conduction number. They indicated that under specific conditions ($M<0.01$), the effect of axial heat conduction can be neglected. However, Lin et al. (2016) and Zhang et al. (2010) stated that, M can be inadequate to judge whether the effect of the axial heat conduction on heat transfer if the uniform outside wall temperature boundary condition was existing. Moreover, Hetsroni et al. (2005) stated that the effect of axial heat conduction can be ignored when $Re<150$ and $M=0.01$. However, axial heat conduction should be considered when $Re>150$ and $M>0.01$. In addition, the effect of axial heat conduction is neglected in the studies of Cole and Cetin (2011) and Yu et al. (2018) for high Pe number values ($Pe>100$). Cole and Cetin (2011) also stated that thermal conductivity of the wall should be lower than the thermal conductivity of the fluid to neglect axial conduction. Furthermore, Barisik et al. (2015) stated that the effect of axial heat conduction can be ignored in pipe flow even for relatively small Peclet number values ($Pe<100$) with the existence of viscous dissipation. The effect of axial heat conduction changes with respect to Knudsen number, Peclet number, thermal conductivity and thickness of the separating wall (Rahimi and Mehryar, 2012). An increment in Kn number, Pe number and hydraulic diameter decrease axial heat conduction rate (Kalyoncu and Barisik, 2016). In contrast, the effect of axial heat conduction on heat transfer increases as Re number, thermal conductivity and thickness of the separating wall increase (Cole and Cetin, 2011). At the entrance region, presence of axial heat conduction increases heat transfer rate. However, axial heat conduction result in reduction in Nu number in fully developed region (Huang et al., 2014). Lin and Kandlikar (2012) stated that the effect of axial conduction can be neglected if the conductivity of channel material is lower than thermal conductivity of the fluid as indicated in the study of Cole and Cetin. (2011) In addition, Kakac et al. (2011) proved that the effect of axial heat conduction can be neglected when Kn number greater than 0.1 and temperature difference between the wall and fluid exceeds 1.667 ($\kappa=1.667$). In Figure 2.19, the effect of axial heat conduction on the heat flux distribution along the wall is represented schematically (Rahimi and Mehryar, 2012). The figure shows that axial heat conduction yields heat flux distribution to vary along the solid-fluid interface even though applied heat flux to the solid region is uniform.

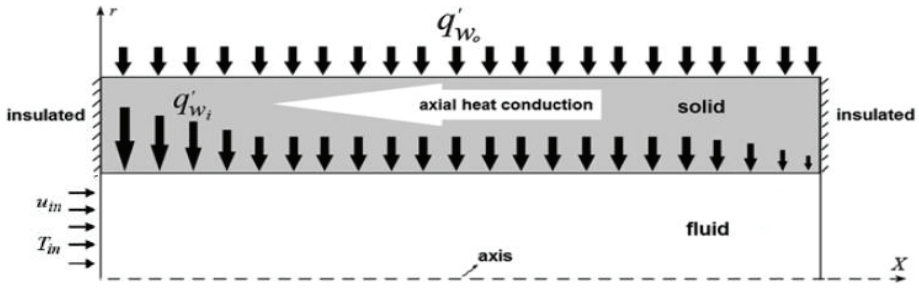

Figure 2.19. Schematic representation of the effect of axial heat conduction on the wall heat transfer per unit length (Source: Rahimi and Mehryar, 2012)

2.3.1.4. Aspect Ratio (AR)

Channel aspect ratio definition varies the literature. Generally accepted definition is the division of channel height to channel width. The orientation of the channel is not crucial for fluid flow due to fixed cross-sectional area (Steinke and Kandlikar, 2006). However, channel orientation cannot be ignored for heat transfer, and it is critical to define heat transfer boundary conditions (Rosa et al., 2009; Zhimin and Fah, 1997). In the rectangular cross sections, Nusselt number depends on the aspect ratio (AR), and Nu increases from square channels ($AR = 1$) to deep rectangular channels (for parallel plates, $AR = 0$) (Rosa et al., 2009). Zhimin and Fah (1997) numerically studied optimization of rectangular microchannels. They stated that channel aspect ratio in laminar flow region must be as high as possible to obtain minimum thermal resistance. They also indicated that the lowest thermal resistance can be achieved in turbulent region; however, this is not preferred because of high pumping power requirements. Furthermore, numerically showed that low thermal resistance (<0.1 W/mK) and high pressure drop (>250 kPa) in microchannels are obtained for high aspect ratio (20.333) and small hydraulic diameter (0.172). In addition, they concluded that the rectangular MCHS with the aspect ratio range of 8.904-11.442 have the best performance in terms of heat transfer and pressure drop. The change in friction factor with respect to aspect ratio was studied by Sahar et al. (2017) and Kim and Kim (2006). According to them, friction factor decreases as aspect ratio increases from 1 to 2, then it starts to increase as aspect ratio keep increasing.

2.3.1.5. Viscous Dissipation

Pressure drop in MCHS are relatively greater than macro scale ones. Therefore, viscous heating effect cannot be neglected as in macro scale heat sinks. Brinkman (Br) number is the ratio of viscous heating overheat conduction in the fluid domain which flows along microchannel, and it is used to determine the effect of viscous dissipation on heat transfer mechanism in MCHS (Çetin et al., 2008). Kalyoncu and Barisik (2016) numerically showed that viscous dissipation increases and decreases heat transfer rate for positive and negative Br cases, respectively. However, they indicated that developed Nu number values are the same for both cases. Morini (2005) stated that decrease in friction factor as Re number increases can be explained with the reduction of viscosity because of viscous heating effect in MCHS. He also stated that viscous dissipation effect become significant for liquid flow when the hydraulic diameter is smaller than 100 μm. In addition, Koo and Kleinstreuer (2004) documented that viscous dissipation should not be ignored for small size channels (d_h<50 μm). Chen (2006) stated that Nu number increases in the fully developed region with viscous dissipation when the value of Kn number is small (<0.03). In contrast, Morini and Spiga (2007) numerically indicated that heat transfer in MCHS is adversely affected by viscous heating due to reduction in Nu number. In addition, Mukharjee et al. (2017) stated that Nu number is inversely proportional to the Br number for constant heat flux boundary condition. Furthermore, Zhai et al. (2017) stated that the effect of viscous dissipation on temperature rise is insignificant when compared to convective heat transfer for water flow. In addition, they also stated that flow distribution and temperature field is affected by the length of entrance region. In order to eliminate entrance effect and obtain more uniform flow field, entrance length should be as long as possible. Morini (2006) stated that at high Re number (>1000), entrance effect with viscous dissipation needed to be considered in order to define flow characteristic and temperature field correctly. In addition, Fani et al. (2015) stated that the effect of viscous dissipation become more important with increasing the Re number and volume fraction.

2.3.2. Uncertainties in Experimental Studies and Summary of the Literature

The results of experimental studies in the literature which are based on MCHS do not consistent with each other. There are three main reasons behind the obtain different results from the experimental studies: (i) fabrication of microchannels (Zhao et al., 2016; Xu et al., 2000), (ii) errors in measurement, (iii) misalignments in the experimental setups. Pfund et al. (2000) emphasize the uncertainties in the experimental studies, and they stated that in order to understand phenomes in micro level correctly, we need to do more precise experiments. Some researchers stated that experimental results are good agreement with theoretical results and conventional correlations can be used at micro scales (Morini and Spiga, 2007; Mukherjee et al., 2017; Zhai et al., 2017; Morini 2006). Missaggia et al. (1989) experimentally confirmed that the utilization of microchannels in the cooling of a laser diode which dissipates 500 W/cm^2 heat flux. They also stated that experimental values are in good agreement with the theoretical calculations.

To sum up, the effect of some physical phenomena (ignored at macro scale) on heat transfer and fluid flow become significant in micro scale studies. In order to evaluate heat transfer and fluid flow characteristics accurately, these phenomena should be considered.

2.3.3. Microchannel Heat Sink for Battery Cooling

Microchannels are rarely used in the cooling of battery cells. In table 2.4, some of studies related to MCHS cooling for battery systems are listed. The application of MCHS for the cooling of battery cells is carried out in two ways: internal cooling and external cooling. In the internal cooling, MCHS with liquid electrolyte are embedded through the electrodes (Mohammadian et al., 2015; Mohammadian and Zhang, 2018). In the external cooling, MCHS are integrated and assembled through the surface of battery cells. Various types of fluids can be used as coolant such as water, ethylene glycol and etc. in the external cooling. The researcher state that internal cooling is more effective than external

cooling in the cooling of battery cells and obtain uniformity through the battery surface. In the study of Pan et al. (2019), MCHS is used to cool battery cells. They emphasize that pressure drop in MCHS is the key factor in the cooling applications, and new designs are required to reduce pressure drop in MCHS by using manifold designs and etc.

The literature shows that, the main concern in MCHS is higher pressure drop values and it should be considered in the design of a cooling system for batteries. Therfore, a numerical study is conducted to figure out the heat transfer and pressure drop characteristics of MCHS by inserting micro fins and nanofluids. According to the results of the numerical study and outcomes of the review study, we decided to design a cooling system in conventional scales for the thermal management of battery cells.

Table 2.4. MCHS for battery cooling

Study	Method	Battery Type	Cooling Method	Coolant
Mohammadian et al., (2015)	Numerical	Prismatic Lithium-ion	Internal External	liquid electrolyte /water
Pan et al., (2019)	Experimental	Lithium-ion	External	water
Mohammadian and Zhang, (2018)	Numerical	-	Internal	liquid electrolyte
Bandhauer and Garimella, (2013)	Experimental	Lithium-ion	Internal	PCM
Liu et al., (2016)	Experimental /Numerical	Prismatic Lithium-ion	External	-

CHAPTER 3

HEAT TRANSFER ENHANCEMENT IN MICROCHANNEL HEAT SINK: NUMERICAL STUDY

Heat transfer and fluid flow characteristic in MCHS are investigated detailly in Chapter 2. The feasibility of MCHS can be measured by the comparison of two parameters; (i) increase in heat transfer rate and (ii) increase in pressure drop. A numerical study on heat transfer enhancement in MCHS is conducted and results are tabulated in this part. Micro pin fins and nanofluids are used to increase the heat transfer rate in MCHS.

Here, we show that overall thermal conductance in a rectangular microchannel heat sink can be maximized with the combination of nanofluids and micro pin fins. We uncover the effect of micro pin fins and nanofluids both separately and simultaneously in order to uncover their effect on the thermal conductance (i.e., thermal resistance).

Advanced applications with miniature designs require great volumetric heating capabilities. Therefore, the literature focuses on maximization of thermal conductance (i.e., minimization of thermal resistances) when the reserved space for cooling system is limited. The literature also focuses on cooling with nanofluids and phase changing materials due to their capability of increasing thermal conductance (Shafahi et al., 2010; Li et al, 2015; Alshaer et al., 2015; Ma et al., 2015). In addition, the literature documents heat transfer enhancement with micro pin fins (Tuckerman and Pease, 1981; Peles et al., 2005; Kosar et al., 2005; Prasher et al., 2006). Nanofluid suspensions (base fluid + nanoparticles) have greater thermal conductivity relative to their base fluid because of the high thermal conductivity of suspended particles. The rate of enhancement in the thermal conductivity of base fluids is still a hotly debated topic. However, it is well known that the downside of nanofluids is that they increase pressure drop (Choi and Eastman, 1995; Choi et al., 2001; Prasher et al., 2006; Xuan et al., 2003; Nguyen et al., 2008; Anoop et al., 2009). Likewise, the pressure drops along the microchannels with inserted micro pin fins (Adewumi et al., 2013; Prasher et al., 2006; Qu and Siu-Ho, 2008).

Tuckerman and Pease (1981) were first to investigate the performance of silicon based micro pin fins. They documented the pressure drop along microchannels for three distinct square fin designs. However, they did not document the thermal performance of fins. Peles et al. (2005) experimentally uncovered the effect of micro pin fins on heat transfer rate and pressure drop. They documented the parameters which are affecting the overall thermal resistance. They showed that the thermal resistance can be decreased greatly (1.5–2.5 times) with inserted pin fin heat sinks. Koşar et al. (2005) investigated the effect of staggered and inline micro pin fin bundles on pressure drop. They compared the micro scale pressure drop results with the macro scale data which evaluated based on conventional pressure drop correlations. In addition, they proposed a modified correlation for flow over micro pin fin bundles. Adewumi et al. (2013) documented what the size of embedded micro pin fins should be to minimize thermal resistance. Prasher et al. (2006) experimentally uncovered the thermal and hydraulic performances of silicon-based, low aspect ratio micro pin fin bundles under cross flow. They showed how the average Nusselt number (Nu) and friction factor vary relative to the fin diameter. Qu and Siu-Ho (2008) surveyed how the heat transfer rate and pressured drop vary with micro pin fin arrays. First (Qu and Siu-Ho (2008), Part I), they proposed two Nusselt number correlations and compared them with the existing correlations. Then (Qu and Siu-Ho, 2008, Part II), they developed a power-law type correlation to predict average Nu number for adiabatic and diabatic conditions.

Nanofluids were introduced by Choi and Eastman (1995). They observed the that the average thermal conductivity of a fluid with suspended copper particle increases. Choi et al. (2001) showed that the thermal conductivity of a base fluid increases approximately two times by addition of less than 1% carbon nanotubes. Prasher et al. (2006) documented how the viscosity of alumina-based nanofluid is affected by shear rate, temperature, nanoparticle diameter and volume fraction. They concluded that increase in the viscosity is greater than (50%) the increase in the thermal conductance. Xuan et al. (2003) experimentally uncovered the enhancement in the thermal conductivity of a copper and water suspension. They also investigated the effect of particle aggregation on thermal conductivity of nanofluids. Nguyen et al. (2008) documented the dynamic viscosity of Al_2O_3/water nanofluid for the temperature range of 20ºC to nearly 75ºC. Anoop et al. (2009) investigated the heat transfer enhancement in laminar developing region for various size and concentration of nanoparticles. Das et al. (2006) comprehensively reviewed the nanofluid literature. They stated that there is not a certain equation nor

approach which gives the change in the thermal conductivity with nanoparticle addition to a base fluid. Buongiorno et al. (2009) emphasized that the literature does not agree on the thermal properties of nanofluids. In order to resolve inconsistencies, an international nanofluid property benchmark exercise (INPBE) was launched at the first scientific conference which focuses on nanofluids. By this way, it was agreed that thermal conductivity and other properties of nanofluids would be tested by over 30 organizations worldwide; and the results would be reported by publications. Chandrasekar et al. (2010) measured the thermal conductivity and viscosity of Al_2O_3/water nanofluid in the volume fraction range from 0.33% to 5%. They concluded that both properties increase linearly as the volume concentration increases. In addition, increase in the viscosity becomes nonlinear after 2% volume concentration because of the hydrodynamic interactions between nanoparticles and base fluid. Later, Chandrasekar et al. (2011) uncovered the change of pressure drop under constant heat flux condition in the plane tube with a 0.1% volume fraction nanofluid (Al_2O_3-water suspension). They observed 34% increase in the Nusselt number; and they did not observe a significant increase in the pressure drop with nanofluids compared to distilled water. Lin et al. (2014) numerically surveyed pressure drops and heat transfer rate of nanofluids (water/Al_2O_3 suspension) in turbulent pipe flow. They stated that distribution of nanoparticles in the flow field becomes nonuniform due to the particle convection, diffusion, coagulation and breakage. They observed Nusselt number decreased by 8% and 3% because of the nonuniformity with Reynolds numbers of 5000 and 25000, respectively. Yuan et al. (2018) numerically uncovered how the volume fraction of cylindrical nanoparticles affect the viscosity of the nanofluid. They showed that resistance to the fluid flow increases with volume fraction; however, the effect of volume fraction diminishes when Reynolds number is greater than 200. Ghanbarpour et al. (2014) experimentally uncovered the thermal properties and rheological behaviour of water based Al_2O_3 nanofluids. They showed that thermal conductivity and viscosity of nanofluids increase as temperature and/or particle concentration increase. However, they documented that the increase in the viscosity is more pronounced than the increase in the thermal conductivity. Karimzadehkhouei et al. (2018) numerically and experimentally investigated the effect of inlet temperature of Al_2O_3 suspension on heat transfer rate along microchannels. They concluded that the effect of inlet temperature on the heat transfer rate is dominant near the inlet of channels (<L/5). The current literature shows that both fins and nanofluids increase the resistance to fluid flow and decrease the resistance to heat flow. However, it focuses on the effect

of micro pin fins and nanofluids separately. Here we uncover what should be the ratio of solid volume reserved for fins and nanoparticles when they both exist in order to enhance the overall thermal conductance (minimization of thermal resistance) with minimum pressure drop. Recent studies emphasize that the nanofluid thermofluidic properties should be measured via experiments, such as thermal conductivity, viscosity etc. Therefore, here we benefit from the experimental results of Chandrasekar et al. (2010).

3.1. Numerical Model

The physical model consists of a microchannel with length scales of $L \times W_c \times H_c$, which is inserted in a silicone substrate with length scales of $L \times W \times H$ as shown in Figure 3.1. Figure 3.1(b) shows how the micro pin fins are inserted into the microchannel and first micro pin fin is located at the inlet of the channel. The material of the micro pin fins is highly conductive silicon substrate. The micro pin fins are circular cylinders with diameter of D_{fin} and height of H_{fin}. The volume of the microchannel is fixed, and so is the volume of the solid domain surrounding it. Length scales of the computational domain are given in Table 3.1.

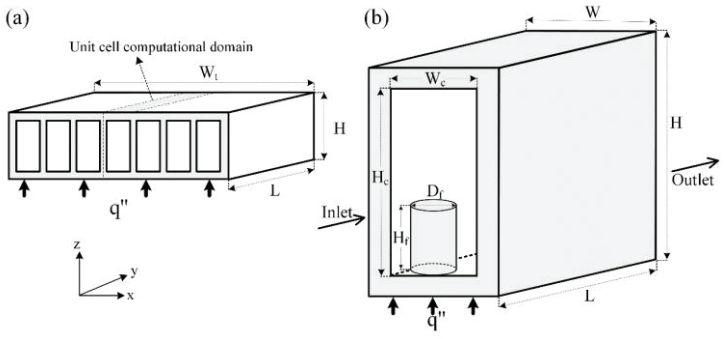

Figure 3.1. Physical model of microchannel heat sink: (a) stacked model and (b) computational domain

Table 3.1. Dimensions of the solid and fluid domains

Solid Domain			Fluid Domain	
H (mm)	W (mm)	L (mm)	H_c (mm)	W_c (mm)
0.9	0.1	10	0.705	0.06

Two physical models were used in the present study. First one is the microchannel heat sink without micro pin fins and the second one is with them, i.e. integrated design.

The volume of the computational domain is fixed, which is

$$L \times W \times H = 9\ mm^3 \tag{3.1}$$

The number of fins inserted into the microchannel can vary but total fin volume is fixed,

$$\forall_{fin,t} = \forall_{fin,1} + \forall_{fin,2} + \cdots + \forall_{fin,n} = 6.03 \times 10^{-4}\ mm^3 \tag{3.2}$$

The height (H_{fin}) and the diameter of the fins (D_{fin}) are 0.08 mm and 0.04 mm, respectively. The total fin volume is 0.14% of the total solid volume.

3.1.1. Governing Equations

The coolant in the simulations is pure water or nanofluid (water-Al_2O_3 suspension). Water and nanofluid are incompressible with homogeneous and constant thermophysical properties. The effect of buoyancy forces is negligibly small in the current problem due to the micro length scales.

Conservation of mass, momentum and energy equations were solved numerically to determine velocity and temperature distribution for the solution domain. For laminar and steady flow, the governing equations are:

$$\nabla . \vec{v} = 0 \tag{3.3}$$

$$\rho_f (\vec{v} . \nabla \vec{v}) = -\nabla P + \mu_f \nabla^2 \vec{v} \tag{3.4}$$

$$\rho_f c_{p,f}(\vec{v}.\nabla T) = k_f \nabla^2 T \tag{3.5}$$

where $\rho_f, c_{p,f}, k_f, \mu_f$ are the density, specific heat, thermal conductivity and dynamic viscosity of the fluid. $\vec{v}$ is the velocity vector in the fluid domain.

For solid regions, the energy equation reduces to:

$$k_s \nabla^2 T = 0 \tag{3.6}$$

where k_s is the thermal conductivity in the solid domains (i.e., the thermal conductivity of solid channel and fins).

3.1.2. Boundary Conditions

The coolant is driven by the pressure difference in between the inlet and outlet surfaces of the microchannel as shown in Figure 3.1(b). The pressure difference between inlet and outlet of the microchannel is defined with respect to the Bejan number. Bejan number (Bhattacharjee and Grosshandler, 1988; Petrescu, 1994) represents the dimensionless pressure difference along a channel and it is symbolized as Be. It was derived during the channel size optimization in forced convection. Furthermore, Bejan and Lorente (2008) are emphasized that the role played by the Rayleigh number for the natural convection cooling is played by Bejan number in forced convection, cf. pp. 92 of Reference (Bejan and Lorente, 2008). Be number is defined in Petrescu (1994) as

$$Be = \frac{\Delta P. L^2}{\mu. \alpha} \tag{3.7}$$

Equation 3.8 is used to determine the pressure difference in between the inlet and outlet surfaces of the microchannel.

$$P_{in} = \frac{Be.\alpha.\mu}{\forall^{2/3}} + P_{out} \tag{3.8}$$

In Equation 3.7 and 3.8, α, ∀, and P_{out} are representing thermal diffusivity of the fluid, volume of the computational domain and pressure at the microchannel outlet, respectively. In addition, the boundaries of the microchannel surrounded by the solid surface is defined as no slip wall boundaries with stationary wall

$$u = v = w = 0 \tag{3.9}$$

The outlet boundary is defined as pressure outlet (at $y=L$),

$$P_{out} = P_{atm} \tag{3.10}$$

The temperature of the coolant at the inlet boundary (at $y=0$) is fixed.

$$T_{in} = 20℃ \tag{3.11}$$

The left and right boundaries of the domain (at $x=0$ and $x=W$) are symmetry boundaries,

$$\partial T/_{\partial x} = 0 \tag{3.12}$$

At the bottom wall (at *z=0*), uniform heat flux is applied,

$$q^{"} = k_s \frac{\partial T}{\partial z} = 10^6\ W/m^2 \tag{3.13}$$

The remaining outside walls of the solid domain surrounding the microchannel are adiabatic. The continuity of energy at the interfaces of solid and fluid surfaces satisfies

$$k_s \frac{\partial T}{\partial n}\Big|_{wall} = k_f \frac{\partial T}{\partial n}\Big|_{wall} \tag{3.14}$$

where n is the outward normal vector.

3.1.3. Nanofluid

Density, specific heat, viscosity and thermal conductivity of the working fluid are function of volume fraction of the suspended nanoparticle. The effective density and specific heat values for nanofluids calculated from the following equations (Pak and Cho, 1998):

$$\rho_{eff} = \emptyset\rho_s + (1 - \emptyset)\rho_f \tag{3.15}$$

$$C_{p,eff} = \emptyset C_{p,s} + (1 - \emptyset)C_{p,f} \tag{3.16}$$

where Ø is the volume fraction of the nanoparticle.

One of the important thermophysical parameters of nanofluids is viscosity which affects the pressure drop. Viscosity of a nanofluid depends on nanoparticle volume fraction, its diameter and temperature (Prasher et al., 2006). Similarly, nanoparticle size, shape, temperature, particle interaction between the solid and fluid are the main parameters affecting the thermal conductivity of the nanofluids (Das et al., 2006; Meyer et al., 2016). In the literature, there are many equations to calculate effective viscosity and thermal conductivity of nanofluids. However, the literature shows that the nanofluid material properties vary dramatically between models in published documents. Experimentally measured nanofluid thermophysical properties were used during the study (cf. experimental results of Chandrasekar et al., 2010) in order to understand the effect of nanofluids in the heat transfer enhancement clearly without the effect of bias in the material model. Thermophysical properties of the base fluid (water) and nanoparticles (Al_2O_3) are given in Table 3.2 (Chandrasekar et al., 2010; Pak and Cho, 1998; Das et al., 2003).

Table 3.2. Thermophysical properties of water and Al_2O_3 at 20ºC

(Source: Chandrasekar et al., 2010; Pak and Cho, 1998; Das et al., 2003)

	k (W/m.ºC)	ρ (kg/m^3)	C_p (J/kg.ºC)	μ (kg/m.s)
Water	0.6	997	4170	0.001
Al_2O_3	35	3880	729	-
Nanofluid (0.1%)	0.621	1025.8	4135.6	000110
Nanofluid (0.2%)	0.630	1057.7	4113.5	0.00121
Nanofluid (0.3%)	0.658	1083.5	4066.8	0.00140
Nanofluid (0.4%)	0.695	1112.3	4032.4	0.00170

3.2. Numerical Procedure

In the numerical part, the conservation of mass, momentum and energy equations were solved numerically by using a commercial finite element software, COMSOL Multiphysics 5.0 (COMSOL, 2014). In the numerical study, flow is laminar and steady state conditions is exist. The computational domain was meshed using free tetrahedral and pyramid elements. The convergence criteria were specified as 10^{-5} for continuity,

momentum and energy equations during the simulations. The simulation results are considered as mesh independent when the criterion of Equation (3.17) is satisfied.

$$\gamma = \left[\frac{(\Delta T)_i - (\Delta T)_{i-1}}{(\Delta T)_i}\right] \leq 0.01 \tag{3.17}$$

Here, ΔT is defined as the difference between maximum and minimum temperatures of the fluid, and "i" represents the mesh index

The effect of mesh size on the simulation results of base model and integrated model are represented in Tables 3.3 and 3.4, respectively.

Table 3.3. Grid refinement test results for base model

Number of Mesh Elements	ΔT (K)	$\left[\frac{(\Delta T)_i - (\Delta T)_{i-1}}{(\Delta T)_i}\right]$
37782	14.9329	-
86867	15.1366	0.0135
264372	15.3619	0.0147
460318	15.4670	0.0068

Table 3.4. Grid refinement test results for integrated design

Number of Mesh Elements	ΔT (K)	$\left[\frac{(\Delta T)_i - (\Delta T)_{i-1}}{(\Delta T)_i}\right]$
51893	14.7852	-
230569	14.9877	0.0135
438920	15.1653	0.0117
585770	15.1812	0.0010

3.2.1. Validation of the Model

Validation of the model is carried out with respect to the literature. Figure 3.2 shows the comparison between the results of Adewumi et al. (2013), Bello-Ochende et al. (2010), and the present study. The accuracy of Adewumi et al. (2013) and Bello-Ochende et al. (2010) were given as 10% and 15% with respect to the analytical results

of Khan et al. (2006) and experimental results of Tuckerman and Pease (1981), respectively. The figure shows that the values obtained in the present study are in good agreement with the studies of Adewumi et al. (2013) and Bello-Ochende et al. (2010) with an average deviation of about 7.3% and 2.6%, respectively.

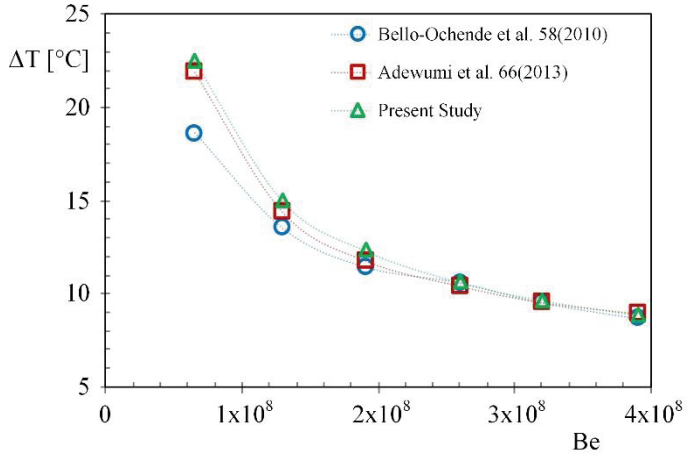

Figure 3.2. Comparison between results of present model and literature for wall temperature differences

3.2.2. Heat Transfer Enhancement by Micro Fins

Figure 3.3 shows the effect of inserted micro pin fins on the peak temperature relative to the Be number. The figure reveals that 2.5% improvement was achieved by integrated design relative to the base model. The effect of integrated design on the thermal conductance diminishes as Be number increases. This result implies that at low Be numbers, heat transfer is limited due to low fluid velocity. Fins increase the heat transfer surface area; therefore, the heat transferred in integrated design is greater even the resistance to the fluid flow is greater. In addition, if the pressure drop related with the extended surface dramatically decreases the fluid velocity, then the base model may provide smaller thermal resistance than the integrated design.

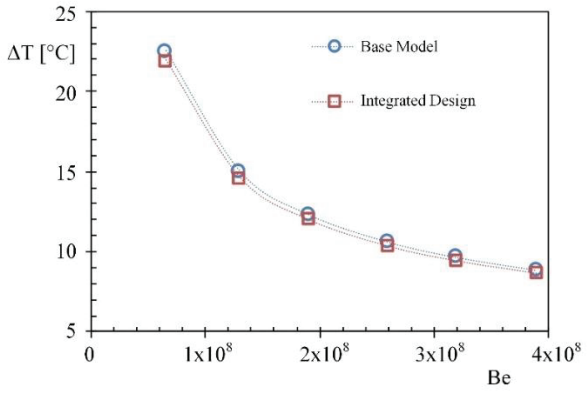

Figure 3.3. Influence of dimensionless pressure drop on the peak wall temperature differences for base model and integrated design

First fin in the integrated design is centred nearly to the inlet of the microchannel and the rest of the fins were aligned with a fixed distance from each other along the microchannel. The optimum fin numbers and the distance between the fins were determined with respect to the minimized peak wall temperature difference. Figure 3.4(a) shows that the peak temperature decreases as the number of fins increases until the 6th fin when $Be = 6.5x10^7$. Then, the peak temperature stands almost steady. Figure 3.4(b),(c) also show that the peak temperature is the smallest for the 6th micro pin fin; and increasing the fin number increases the peak temperature (thermal resistance) afterwards. Overall, according to Figure 3.4, the integrated design with 6 micro pin fins minimizes the peak wall temperature differences (maximum thermal conductance) for low, intermediate, and high Be numbers.

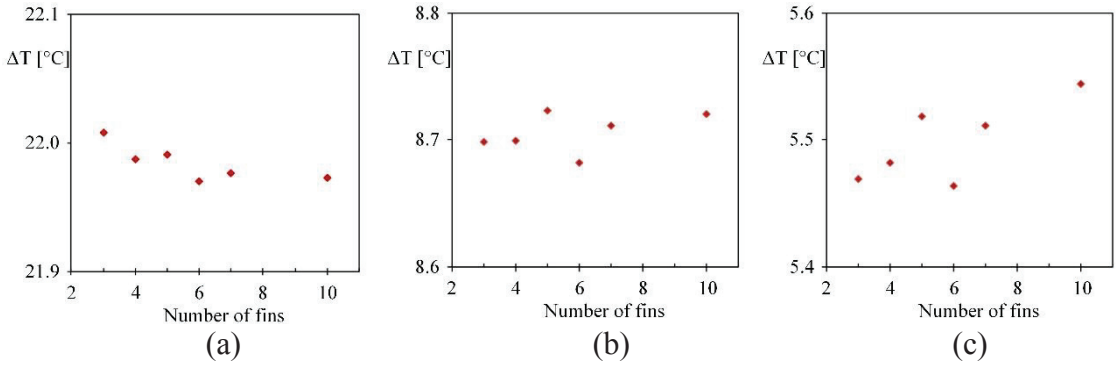

Figure 3.4. Variation of the peak wall temperature differences with fin numbers for: (a) Be=6.5×10^7, (b) Be=3.9×10^8, (c) Be=1.3×10^9

Figure 3.5 shows the effect of distance between the fins on peak wall temperature difference for 6 fins. According to Figure 3.5, the peak wall temperature difference is minimum when the distance between the fins is 0.0825 mm for all Be numbers. In Figure 3.5, it can be seen that the peak wall temperature difference increases as the distance between the fins increases. This result implies that as the distance between the fins increases, the next level of fins stays in the wake of the previous fins due to the increase in the thermal boundary layer. Furthermore, as the fluid flows along the channel its temperature increases, which decreases the heat transfer rate from the fins to fluid. Therefore, the effect of fins on heat transfer rate diminishes as the spacing in between them increases.

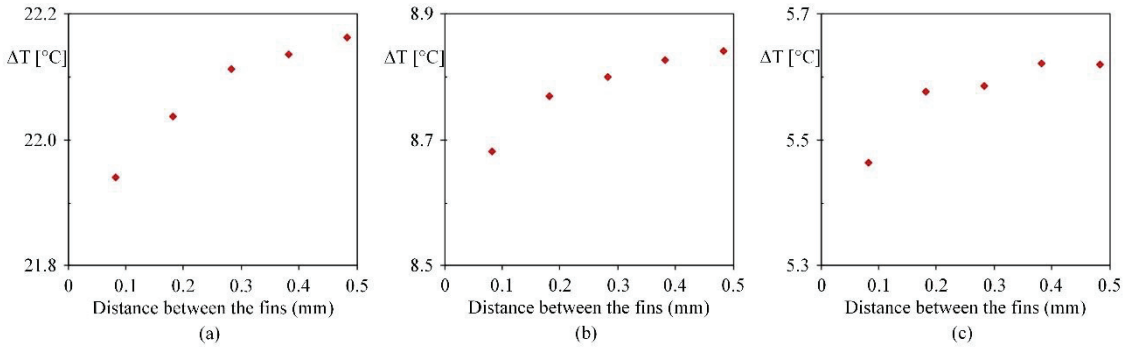

(a) (b) (c)

Figure 3.5. Variation of the peak wall temperature difference with the distance between the fins for: (a) Be=6.5×10^7, (b) Be=3.9×10^8, (c) Be=1.3×10^9

3.2.3. Heat Transfer Enhancement by Nanofluid

Next consider the coolant is a nanofluid (suspension of water and Al_2O_3) with various volume fractions. Figure 3.6 shows that the peak temperature difference decreases with 4% Al_2O_3 nanoparticle addition to the water. The effect of nanofluid on the peak temperature difference is more pronounced at low Be numbers. However, 18% and 25% improvements were observed in minimizing the peak wall temperature difference by using nanofluid for Be numbers 6.5×10^7 and 1.3×10^9, respectively. Note that Be number (dimensionless pressure difference) is fixed throughout the study; therefore,

change in the pressure drop is related to the variation in the material properties as can be seen in Equation 3.7.

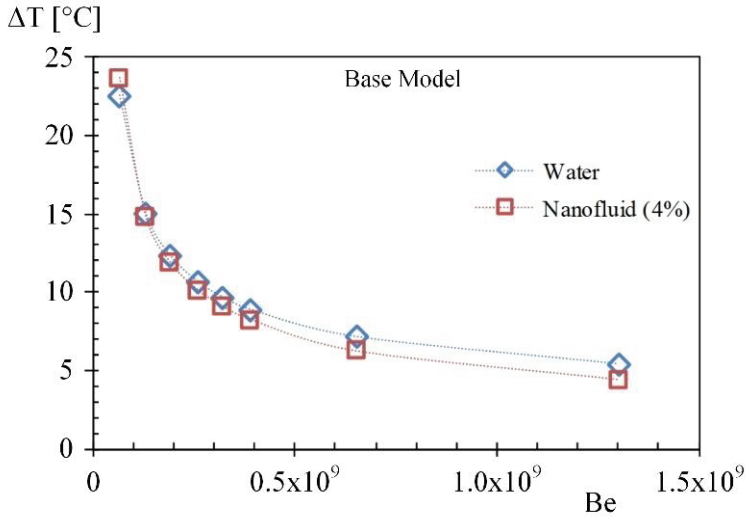

Figure 3.6. Variation of the peak wall temperature difference with Be number for Base Model

Figure 3.7 shows the effect of nanofluid on the peak wall temperature difference for the integrated design. Similar to the base model (Figure 3.6), nanofluid increases the overall thermal conductance for all Be numbers; however, increase in the thermal conductance for the integrated design diminishes as the Be number increases. Maximum improvement in the peak wall temperature difference was measured as 18% for the lowest Be number, 6.5×10^7.

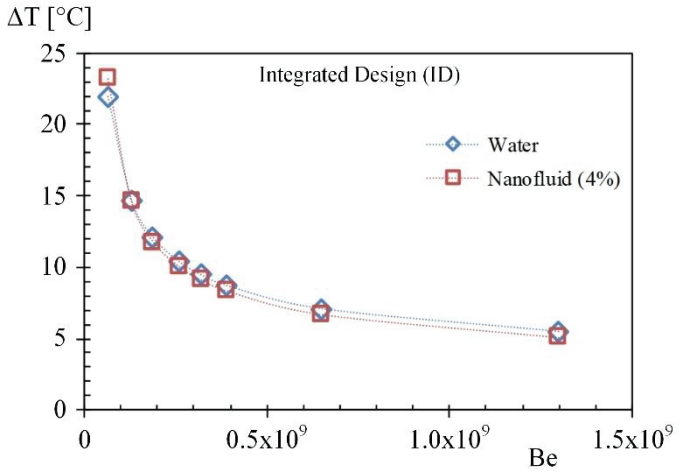

Figure 3.7. Variation of the peak wall temperature difference with Be number for Integrated Design

Comparison of Figures 3.6 and 3.7 reveals that the enhancement in the thermal conductance is greater in base model than the integrated one for the greatest Be number. However, the integrated design yields better enhancement in the thermal conductance as the Be number decreases. This shows that only fins yield better thermal performance at low Be numbers, and only nanofluid at high Be numbers. Therefore, there is an optimal volume fraction ratio at the intermediate Be numbers. The effect of nanofluid volume fraction on the peak wall temperature differences is represented in Figure 3.8(a)–(c) for the lowest, intermediate, and highest Be numbers. Volume fraction of nanofluid varies from 1% to 4%. In general, Figure 3.8(a)–(c) show that thermal conductance increases as the nanoparticle volume fraction in the fluid increases, with the exception of Figure 3.8(a). Figure 3.8(a) is for the lowest Be number case; therefore, increase in the flow resistance limits the enhancement in thermal conductance via nanofluids. The minimum wall temperature differences are observed in 4% volume fraction. The volume fraction was limited as 4% in order to eliminate agglomeration in the nanofluid. Figure 3.8 shows that utilizing nanofluid is an ineffective solution to reduce peak wall temperature differences for the lowest Be number at 1% volume fraction. Maximum improvement in the peak wall temperature difference is 25% in the highest Be number for 4% volume fraction. However, the pressure drop increases dramatically as the volume fraction increases from 1 to 4%, i.e. 10.3% to 45.4% increase compared to the base fluid, respectively.

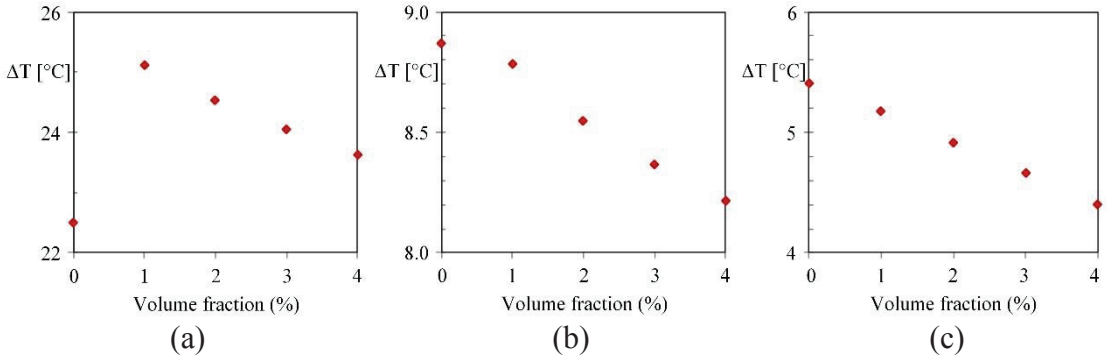

Figure 3.8. Variation of the peak wall temperature difference with nanofluid volume fraction for different Be numbers; (a) 6.5×10^7, (b) 3.9×10^8, (c) 1.3×10^9

The effect of total fin volume and volume fraction of nanofluid on the temperature difference is shown in Figure 3.9. The peak wall temperature difference decreases by increasing the volume fraction of nanofluid while fin volume is fixed. However, increasing the total volume of the fins decreases the thermal conductance. For instance, 3.8% increment in the wall temperature is observed when the fin volume increases eight times. This situation can be explained as an increase in the total fin volume increases the resistance to the fluid flow, which decreases convective heat transfer coefficient.

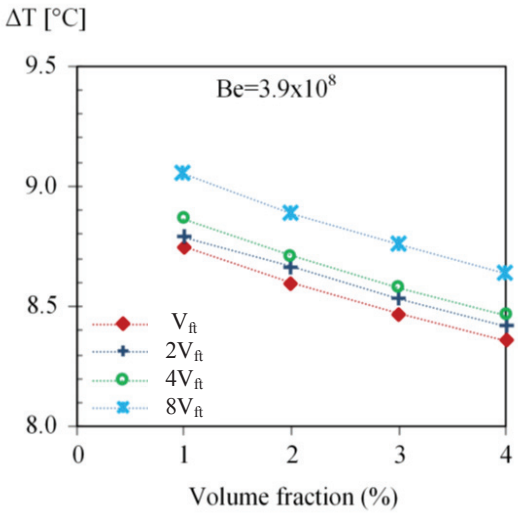

Figure 3.9. Variation of the peak wall temperature difference with volume fraction of nanofluid and total fin volume

Figure 3.10 summarizes the results of the study. According to Figure 3.10, integrated design with nanofluid minimizes the peak wall temperature difference for the lowest Be number. In addition, base model with water yields the greatest peak wall temperature difference for the lowest Be number. Furthermore, base model with nanofluid minimizes the peak temperature difference for the highest Be number. Therefore, it can be concluded that thermal conductance is maximum with fins and nanofluid, and nanofluid for low and high Be numbers. Therefore, nanofluid should be used with or without fins relative to the given Be number in order to maximize the thermal conductance. For instance, if an evolutionary analogy is used, it means that particles forming the fins dissolves in time to enhance heat transfer rate.

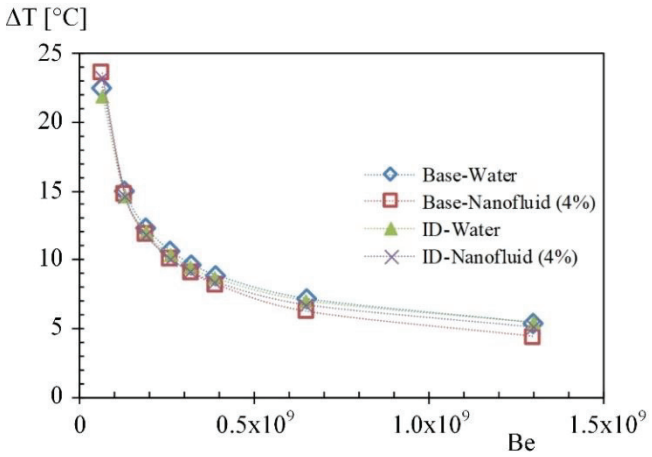

Figure 3.10. The change in the peak wall temperature difference by volume fraction of nanofluid and total fin volume

Next, consider that the thermal conductivities of the nanoparticle and fins are the same (35 W/m.K) in order to understand the evolutionary concept. Figure 3.11 shows how the temperature difference and volumetric flow rate vary relative to the Be number for fins, nanofluids and fins + nanofluids with fixed volume fraction. So far, the fin volume was 0.14% and the maximum nanofluid volume fraction was 4%. Here, the summation of the volumes of fins and nanoparticles correspond to 4.14% volume fraction. Therefore, the optimal ratio of volume fraction between the fins and nanofluid for thermal conductance enhancement becomes evident.

According to Figure 3.11, nanofluid yields the maximum thermal conductance (almost 50% improvement in the thermal conductance relative to the micro pin fins) by minimizing the peak wall temperature difference. Figure 3.11(a) shows that the thermal conductance with only fins (4.14% volume fraction) is smaller in comparison to the only nanofluid (4.14% volume fraction) whereas their resistance to the fluid flow is greater (decreased volumetric flow rate "$\dot{\forall}$" for the same Be number). Figure 3.11(a)–(b) shows that suspending the majority of the solid volume into the fluid enhances thermal conductance more than embedding micro pin fins; and it also minimizes resistance to the fluid flow. However, Figure 3.11(a), (b) also shows that greatest thermal conductance and the smallest resistance to the fluid flow is achieved when a small percentage (0.14% volume fraction) of the solid volume is reserved for fins.

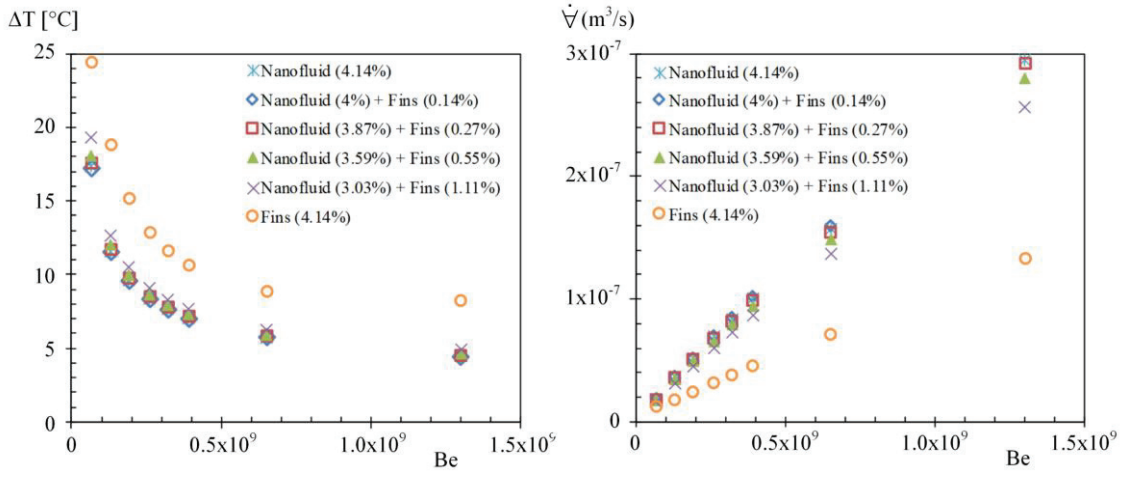

(a) (b)

Figure 3.11. The change in (a) the peak wall temperature difference and (b) the volumetric flow rate of the coolant with respect to volume fraction of nanofluid and total fin volume

3.3. Discussion of the Numerical Results

Here, we document what should be the volume fractions of micro pin fins and nanoparticles to conform maximum thermal conductance for a microchannel heat sink. The effect of fins and nanoparticles suspended to the base fluid (water) on the thermal

conductance documented both solely and simultaneously. The results show that microchannel with micro pin fins provides greater thermal conductance than microchannel without micro pin fins. The distance between the fins and their number were optimized to maximize thermal conductance. Heat transfer enhancement with nanofluid is also documented for various Be numbers. The results show that nanofluid with volume fraction of 4% significantly reduce the peak temperature. Nanofluid with any volume fraction improve the thermal conductance for all the surveyed Be numbers. However, nanofluid also increases the resistance to the fluid flow which requires additional pumping power. Nanofluid with micro pin fins increases the thermal conductance by 18% for the lowest Be number relative to the base fluid without fins. Increase in the total fin volume increases the resistances to the fluid flow, and therefore it increases the temperature difference of the microchannel up to 3.8%.

Nanofluid decreases the peak temperature more than inserting micro pin fins when the thermal conductivity of nanoparticles and micro pin fins are the same. Almost 50% improvement is achieved with nanofluid instead of micro pin fins. Overall, the results uncover that there is an optimum volume fraction reserved for fins and nanoparticles suspended in the base fluid for a prescribed set of conditions. Depending on the material properties of substances, the volume fractions which provide the minimum peak temperature (maximum thermal conductance) is affected.

Both nanofluids and micro pin fins decrease the overall thermal resistance due to increase in the average thermal conductivity of the flow system. In addition, they increase the heat transfer surface area of the solid interacting with the fluid. However, the pumping power (pressure drop) increases in both methods due to the increase in the resistances to the fluid flow. The results document what should be the nanoparticle volume fraction mixed into the base fluid and the micro pin fin volume in order to minimize thermal resistance. If the thermal conductivity of the nanoparticles and micro pin fins are the same, the thermal conductance becomes the maximum with 4% and 0.14% volume fractions for the nanofluid and micro pin fins, respectively. This result shows that inserting micro pin fins and using nanofluids with a given volume fraction ratio maximize the overall thermal conductance.

The result of the numerical study is evaluated in terms of heat transfer enhancement and pressured drop values in microchannel heat sink. According to the results, using microchannel heat sink for battery cooling is not feasible because of relatively high pressure drop values which increases the energy consumption in the

electric vehicle thermal management system. Therefore, it is decided to design a new heat exchanger in conventional length scales.

CHAPTER 4

MATERIALS AND METHODS

The methodology of the thesis is mainly based on experimental studies. Firstly, experimental procedure is introduced with utilized components and devices. The experimental part is mainly divided into two sections. They are silicone heater system and real battery case. In the real battery case, experimental studies conducted with a single battery cell and a 3S battery module.

4.1. Experimental Procedure

Experimental part consists of studies related to silicone heater system and pouch cell batteries. The same experimental procedure is followed for the silicone heater system and real battery case. Firstly, the heat generation and temperature profile of battery cells during charging, discharging and operating are investigated in detail via literature review. A silicone heater system which shows the thermal behaviour of the battery cell is created by benefiting from the literature knowledge. An experimental study is conducted on the cooling of the silicone heater system to evaluate the thermal behaviour of battery cell under various discharge rate by applying various heating loads to the silicone heater.

The experimental setup of silicone based system consists of a silicone heater system, a water bath, a thermal camera, a needle valve, a flowmeter, a programmable power supply and a data logger. In addition to these materials, a programmable electronic load is used in the experimental study of the battery cell/module.

In real battery case, a lithium-ion pouch type battery cell with a capacity of 7.5 Ah (Kokam, SLPB705106100) is used (Figure 4.1). The specification of the cell is given in Table 4.1. The allowable continuous charge and discharge conditions are specified as 1C rate and 2C rate, respectively.

Figure 4.1. 7.5 Ah Pouch Cell (Kokam SLPB705106100)

Table 4.1: Specification of Kokam Pouch Cell

Type		SLPB75106100
Typical Capacity		7.5 Ah
Nominal Voltage		3.7 V
Charge Condition	Max. Current	7.5 A
	Voltage	4.2 ±0.03 V
Discharge Condition	Continuous Current	15 A
	Peak Current	37.5 A
	Cut-off Voltage	2.7 V
Operating Temperature	Charge	0 ~ 40ºC
	Discharge	-20 ~ 60ºC
Dimensions	Thickness	7.5 ± 0.2 mm
	Width	106 ± 0.2 mm
	Length	100 ± 0.2 mm
Weight		155 ± 5 g

In the cooling of battery cells, a heat exchanger (HEX) is used. The HEX is designed to control and distribute the temperature of battery cell uniformly (Figure 4.2). The dimensions of the HEX are defined with respect to the battery size. The HEX consists of a main distribution channel, a main gathering channel, two cooling plates and five heat distributing channel. The heat distributing channels are in elliptic shape and they are created by squeezing circular channels from two sides (Figure 4.2(b)).

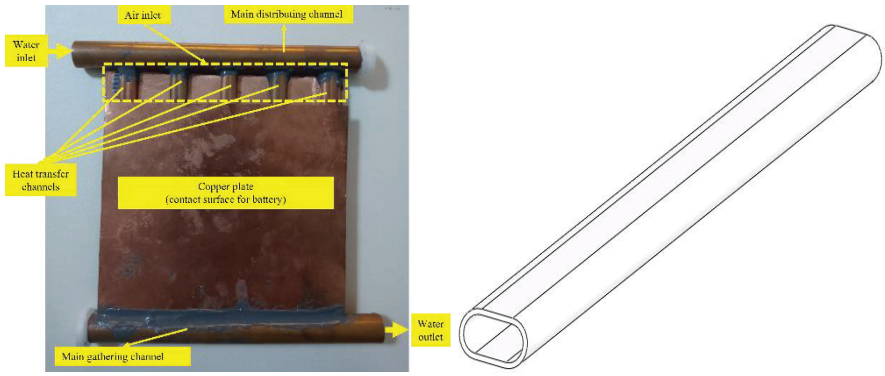

(a) (b)

Figure 4.2. (a) Heat exchanger and (b) heat transfer channel

In the first part of the real battery case, temperature distribution on the surface of a single battery cell is measured by thermocouples and monitored via a thermal camera. Then, a battery module is created by the connection of three lithium-ion pouch cells in serial. According to the results obtained from single battery case, a cooling system consists of a battery module, HEXs and a manifold design is created to allow air and liquid cooling solely and simultaneously. Therefore, the methodology of thesis can be summarized under three headings: studies conducted on silicone heater system, cooling of a single battery cell and cooling of a battery module.

4.1.1. Measurement Devices

In that section, the measurement devices and methods used in the experimental parts are explained in detail. During the measurement campaign, temperature (T) and voltage (V) values in the battery module are measured via thermocouples and stored by a data logger. In the silicone heater system and the single battery cell case, a thermal camera is used to take infrared images during the experiments. The measured data are used to evaluate cooling capacity of the thermal management systems.

Thermocouple measures T and V values with an accuracy of ±1.5°C and ±60 μV, respectively. T and V values are measured every second and stored by HIOKI data logger (Figure 4.3). Technical specifications of the data logger are given in Table 4.2. The data

logger has ten channels and be able to record temperature and voltage values during the experiments. The accuracy of the data logger is ±0.35°C and ±0.2 V for temperature and voltage measurements, respectively.

Figure 4.3. HIOKI Data Logger (LR8431-20)

Table 4.2. Technical specifications of data logger

Type	Hioki Data logger (LR8431-20)
Measurement Range	Temperature: -20°C to 70°C Relative Humidity: 5% to 95%
Accuracy	Temperature: ±0.35°C from 0°C to 50°C Relative Humidity: ±2.5% from 10% to 90%
Memory	64K bytes

4.1.2. Charging/Discharging Procedure

Charging and discharging of battery module are carried out via programmable DC power supply and programmable DC electronic load, respectively. The maximum power outpu of the charger and discharger are 360 W and 1500 W, respectively. The technical specifications of the devices are given in Table 4.3 and they are represented by Figure 4.4 (a)-(b).

Figure 4.4. (a) Programmable DC Power Supply and (b) Programmable DC Electronic Load

Table 4.3. Technical specifications of charger and discharger

	Discharger	Charger
Type/Model	BK Precision 8614	GW Instek PSH2018A
Input Voltage	0-120 V	0-20 V
Input Current	0-240 A	0-18 A
Input Power	1500 W	360 W
Accuracy	±(0.05%+0.1FS)	≤ 0.1%+5 mV ≤ 0.2%+5 mA

Here, the procedures which are followed during charging and discharging of battery cell/module are introduced. The charging process takes place via two steps: constant current (CC) and constant voltage (CV) mode. Firstly, the maximum allowable voltage value for the battery cell (4.2V and 12.6V for a lithium-ion puch cell and 3S battery module, respectively) and output current are adjusted on the programmable DC power supply. The output current represents the charge/discharge rate. The lithium-ion pouch cell/module is started to charge in CC mode and when the voltage of the cell/module reaches its maximum value, the power supply swtiches charge mode from CC to CV. The charging process is completed when the current on the power supply reaches to 0.05% of the battery capacity (i.e. 0.375A for 7.5Ah capacity battery cell). In the discharging process of a battery cell/module a DC electronic load is utilized. Discharging of battery cell/module is carried out in CC mode. The minimum allowable voltage (cut off voltage) and output current can be aligned by the electronic load. The discharging process is completed when battery voltage reaches to minimum allowable voltage which are 2.7V and 8.1 V for a pouch cell and 3S battery module, respectively.

There are some variables used to describe condition of the battery cell during charging and discharging. One of them is the state of charge (SOC) which represents the current battery capacity as a percentage of maximum allowable capacity. SOC is considered during charging process and it is used to estimate change in battery capacity over time. The other one is that the depth of discharge (DOD) which represents the discharged battery capacity as a percantage of maximum capacity [MIT, 2008].

A battery management system (BMS) card is implemented to battery module to control voltage of battery cells. It prevents over charging and discharging of a battery cell in the battery module. A 3S-40A BMS card with its cable connections is shown in Figure 4.5. The charging/discharging of battery cells are carried out via BMS circuits.

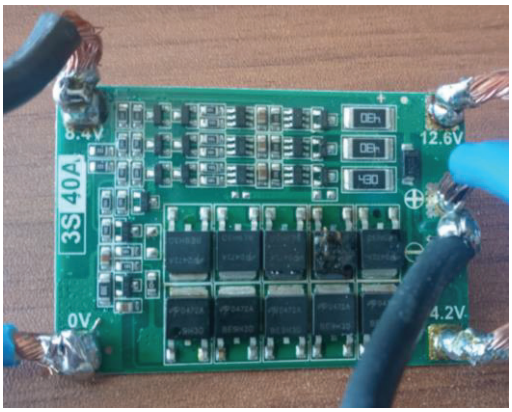

Figure 3.5. 3S-40A BMS Card

4.1.3. Other Equipment

A water bath (Labo C200-H13) supplies coolant liquid to the system at specified temperature and flow rate (Figure 4.6). The technical specifications of the water bath is given in Table 4.4. It operates in the temperature range -20°C to 100°C. The maximum allowable flow rate of water for the water bath is 16 lt/min. In the experimental setup, the flowrate of the coolant is measured by a turbine type flowmeter.

Figure 4.6. Water Bath and technical specifications

Table 4.4. Technical specifications of Labo water supply

Type/Model	Labo C200-H13
Temperature Range	-20/100°C
Heating Capacity	1.1 kW
Cooling Capacity	0.25 kW
Bath Capacity	7 lt
Maximum Flow Rate	16 lt/min
Temperature Stability	±0.03°C

A fan is utilized to supply air at ambient temperature for battery cooling (Figure 4.7). It is located at the inlet of the air manifold and the air flow inside air duct is regulated by honeycombs which are placed along the duct. The power ouput and the allowable flow rate of the fan are specified as 19-22 W and 2.52-2.83 m^3/min, respectively.

Figure 4.7. Tubeaxial Fan

CHAPTER 5

DIFFERENT APPROACHES FOR BATTERY SYSTEMS

5.1. Silicone Heater System

A silicone heater which represents the thermal behaviour of the battery cell (heat generation inside the battery cell and temperature distribution on the surface of the battery cell) is produced with respect to literature studies and it is utilized in the experimental studies. Such a method has not proposed up to now in the literature, so the study may be creating a new experimental procedure for future studies. Also, it enables to conduct studies on battery systems without using real batteries.

The experimental setup for the silicone heater system is shown in Figure 5.1. The main components of the experimental setup are a water bath, a needle valve, a flowmeter, a silicone heater system engaged with a cooling channel, a data logger and a power supply. A water bath supplies coolant liquid to the system. The flow is regulated by a needle valve and flowrate of the coolant is measured via a flowmeter. The silicone heater system and coolant plate are in contact with each other to allow heat transfer, while the remaining surfaces are isolated from the environment. The temperature on the surface of the silicone heater system, temperature of the coolant at the inlet and outlet are measured by thermocouples. All the measured values are recorded via data logger.

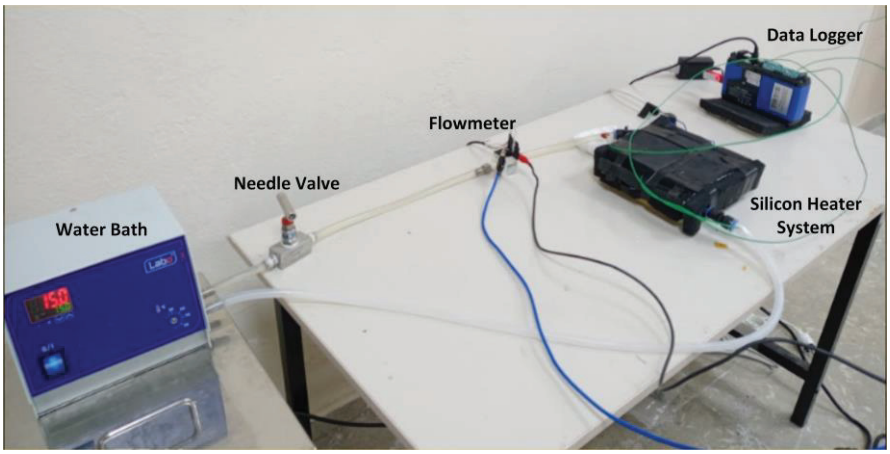

Figure 5.1. Experimental setup for silicone heater system

The heat generation and temperature distribution characteristics of a lithium-ion pouch cell is studied in detail in the Chapter 2. According to that knowledge, a silicone heater system which reflects the thermal behaviour of a pouch cell is created by a silicone heater is located between two steel plates (Figure 5.2). Stainless steel is selected for the metal plate because of its thermal conductivity value. Thus, the thermal conductivity of silicone heater system and the battery cell in thickness direction are almost identical. The silicone heater system is activated by DC power supply. The maximum capacity and working voltage of the silicon heater are 50 W and 20 V, respectively. The heat generated in the silicon heater can be altered by changing the supplied current and this situation approximate discharging of a battery cell at various C-rates.

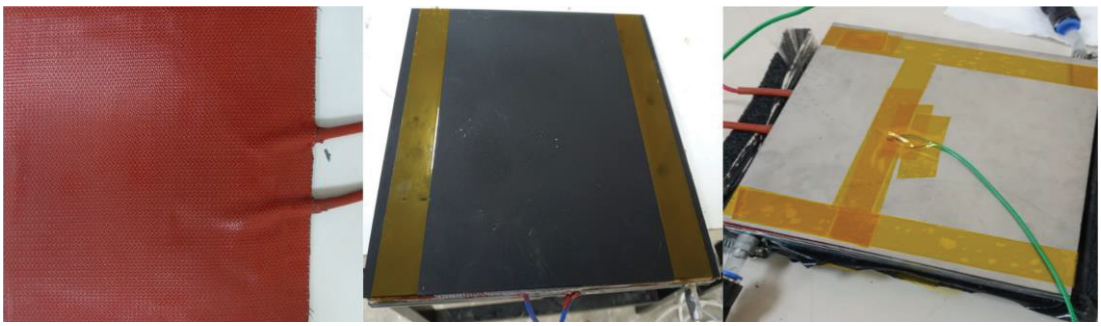

(a) (b) (c)

Figure 5.2. Silicone heater system (a) Silicone heater (b) silicone heater sandwiched between the metal plates and (c) location of thermocouple

5.1.1. Results of Silicone Heater System

The temperature distribution on the surface of silicone heater system is shown in Figure 5.3. The thermal image captured by thermal camera at the middle of the heat generation process when the heat generation rate is 30 W. According to the Figure 5.3, the heat generation is not uniform along the surface of silicone heater system as occurs in batteries. The temperature is dense near the bottom side of the silicone heater system.

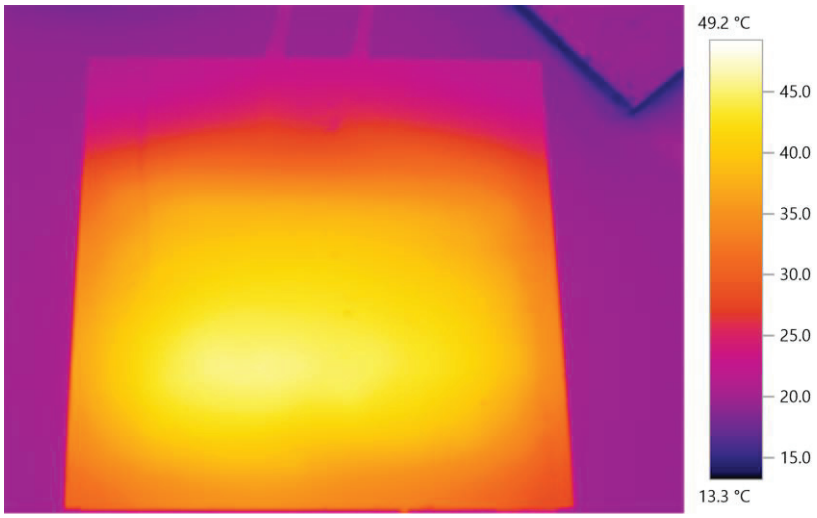

Figure 5.3. Thermal image of temperature distribution on the surface of the silicone heater system

The temperature changes of the silicone heater system under various heating loads (7 W - 48 W) are measured via thermocouples. The aim of generating various heating loads is to simulate thermal behaviour of a real battery under various charge/discharge rate (C-rate) by using silicone heater system. An example from literature shows that the generated heats for a 14 Ah capacity pouch cell are calculated as 7.19 W and 17.95 W during 3C and 5C discharge rate, respectively (Vertiz et al., 2014).

The coolant liquid is supplied to the system with a flowrate of 0.0218 kg/s and at a temperature of 15°C. The change of the temperature on the surface of silicon heater system at various heating loads is given in Figure 5.4. According to the Figure 5.4, the temperature of the silicone heater system can be controlled by using liquid cooling up to

30 W heating load. As a result, the cooling capacity of the system is determined as 30 W for continuous loading. The temperature of the silicone heater system exceeds to 55°C in 10 minutes for 48 W heating load. This means that, if a battery cell discharged at 6C rate (the discharge is completed in 10 minutes), the temperature of the cell has been exceeded the operating temperature limits through the end of the discharge.

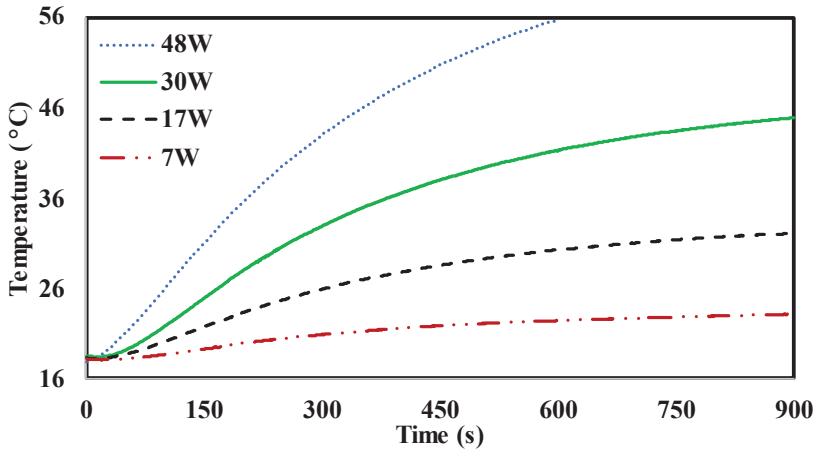

Figure 5.4. The change in temperature values of the silicone heater system under various heating load

The effect of the coolant temperature on the temperature change of silicone heater system when the heating load is 30 W is shown in Figure 5.5. According to the Figure 5.5, the temperature of the silicone heater system reaches to 45°C in 7.5 min when there is not cooling system. This means that the temperature of a battery cell has been reached critical values through the end of the discharging process (8C rate). The temperature of the silicone heater system is kept below 45°C for 15 minutes when the cooling system at various temperature values, i.e., 10ºC and 15ºC, is involved in the process.

Here, thermal behaviour of a battery system is estimated by using silicone heater system under various heating load. The discharge of the battery cell is carried out constant current mode, and it means that there is a continuous load on the battery cell throughout the discharge process. Therefore, a silicone heater system is introduced to estimate thermal behaviour of a battery cell under various discharge rates in the present study.

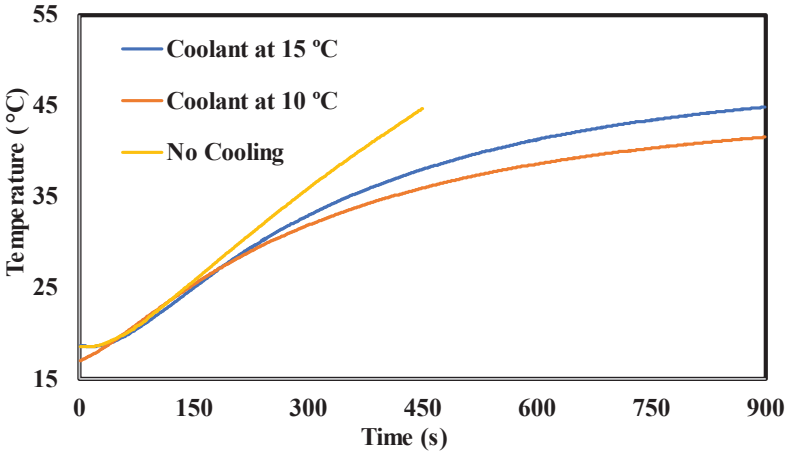

Figure 5.5. Temperature change in the silicone heater system under different conditions

5.2. Single Lithium-ion Pouch Cell

Here, the temperature distribution on the surface of a lithium-ion pouch cell is monitored via a thermal camera and is measured by thermocouples. The experimental setup for single lithium-ion pouch cell consists of a lithium-ion pouch cell, a HEX, a needle valve, a flowmeter, a DC power supply, a DC electronic load, many thermocouples, a thermal camera, and a data logger. Five thermocouples are positioned along the surface of the battery cell to measure temperature change during charging/discharging. Cooling of the battery cell is carried out by using a heat exchanger.

The temperature variations in the surface of the battery cell are monitored by use of thermal camera and simultaneous thermocouple measurements under various charge/discharge rates. There is only natural convection during the measurements. After that, a cooling system is introduced to the battery cell to control temperature values. The precision of the measurement devices is increased by considering the accuracy values given in the data sheets. The locations of the thermocouples on the surface of the battery cell are shown in Figure 5.6. CH1 and CH2 are positioned near to the negative and positive tabs, respectively. CH3 is located at the middle of the battery cell. CH4 and CH5 thermocouples are positioned at the bottom of the battery cell.

Figure 5.6. The locations of the thermocouples on the surface of the battery cell

5.2.2. Results of Single Battery Cell

The battery cell charged at 2C rate, and the temperature distribution on the surface of the battery cell is represented in Figure 5.7. There is not any cooling system during the charge and the ambient temperature is recorded as 30.2ºC. According to the Figure 5.7, the highest temperature values are recorded for CH1 and CH2 (they are positioned near the tabs). In addition, the lowest temperature values are recorded for CH4 which is the outermost points to the tabs. The difference between the maximum and the minimum temperature values is 2ºC for the battery cell. Also, the temperature of the battery cell remains within operating temperature limits and there is only 5ºC increment in the temperature of the battery cell during the charge at 2C rate.

The temperature of the battery cell increases sharply at the beginning of the charging process and decreases through the end of the charging process. These situations can be explained with the mode of the charging process. The temperature of the battery cell increases during CC mode which is occurred at the beginning of the charging process. Then, the charging mode is changed from CC to CV when the voltage of the battery cell reaches to its maximum value. The supplied current to the battery cell decreases during the CV mode. Thus, the decrement in the temperature value through the end of the charging process can be explained with the decrease in the current values at CV mode. The small decrease in the temperature values at the middle of the charging process can be related to chemical reactions occur in the battery cell.

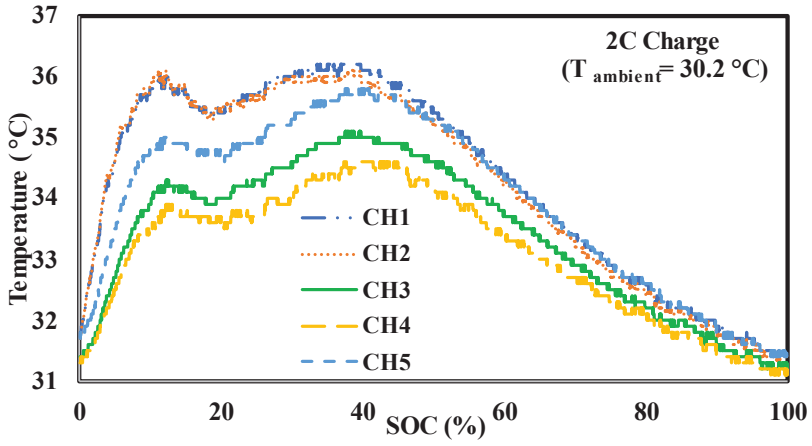

Figure 5.7. The temperature distribution on the surface of the battery cell at 2C rate charging

The change in temperature during 2C and 3C rate discharging process are shown in Figure 5.8(a) and Figure 5.8(b), respectively. The ambient temperature is kept constant (30ºC) during discharging process. According to Figure 5.8(a-b), the temperature of the battery cell increases throughout discharging process. The main reason behind that the nature of the discharging process: discharging process occurs only in CC mode. There is only natural convection as a cooling system during the discharging process. The maximum temperature values are out of the operating limits and measured as 46.1ºC and 51.7ºC for 2C and 3C rate discharge, respectively. Also, the maximum temperature difference between the measurement points is recorded as 5ºC and it is the critical value for operating limits. The highest and the lowest temperature values are measured at near to the negative tab and at the outermost points to the tabs during discharging process, respectively.

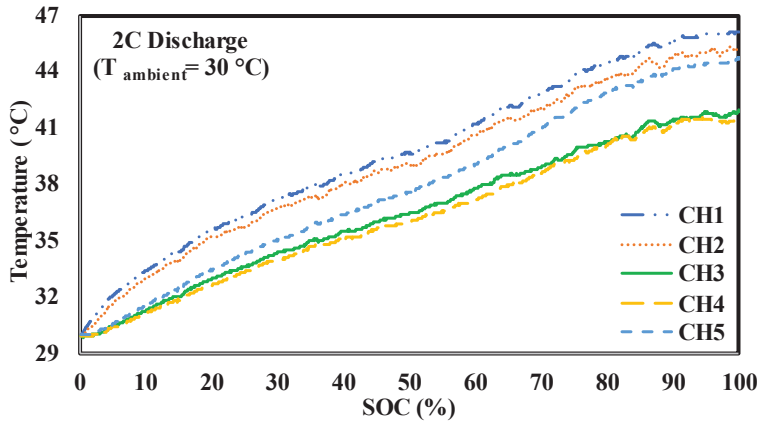

(a)

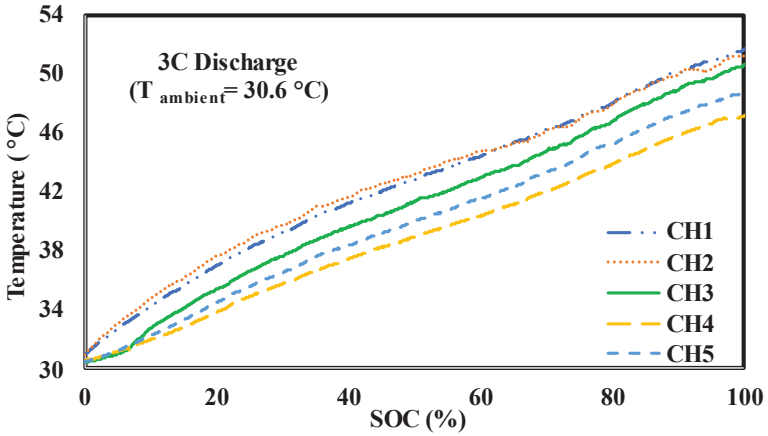

(b)

Figure 5.8. The measured temperature values for the single battery cell during discharge (a) 2C rate and (b) 3C rate

The infrared images of the battery surface are captured via a thermal camera during the charge/discharge. Figure 5.9 (a) and (b) show the temperature distribution on the surface of the battery cell at 424s of the charging and at end of discharging process, respectively. There is only natural convection during the 2C rate charge/discharge. The comparison of thermal images of the battery cell shows that the heat generated during discharge is larger than that by charge. The measured maximum temperature values are 37ºC and 46ºC at 2C charge and discharge rate, respectively. The thermal image obtained at 2C charge rate is captured when the temperature of the battery cell reaches its maximum value.

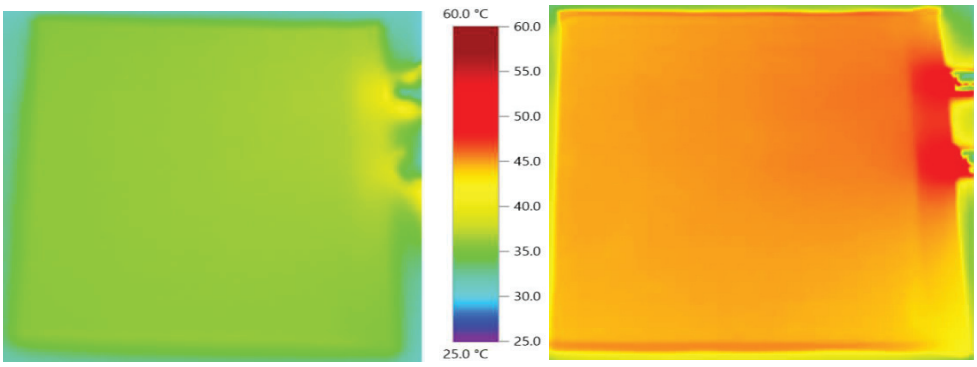

(a) (b)

Figure 5.9. Thermal images of battery cell at 2C rate (a) 424 s of charge and (b) at the end of the discharge

According to Figure 5.7 and Figure 5.9(a), there is a slight increase in the temperature of the battery cell during charging. Thus, a heat exchanger is designed and introduced for battery cell to control the temperature during discharging process. The temperature of coolant liquid is measured as 17ºC at the inlet of the cooling system. The change in temperatures on the surface of the battery cell at 2C discharge rate are monitored by using a thermal camera. Thermal images of battery surface at 2C discharge rate are shown in Figure 5.10 (a-b). According to the Figure 5.10(b), the temperature of the battery cell is kept below the 30°C when the cooling system is introduced to battery cell. In addition, the maximum temperature of battery is 29.2°C. The cooling capacity for the HEX is calculated as 20 W.

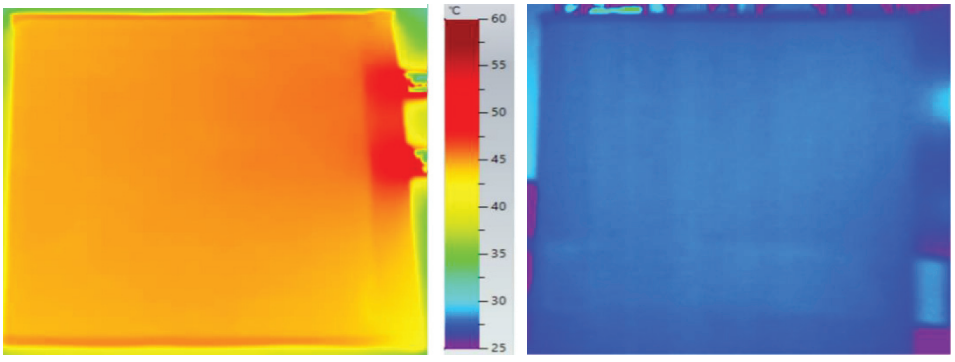

(a) (b)

Figure 5.10. Temperature distribution on the battery surface at the end of the discharge for 2C rate: (a) no cooling (b) liquid cooling

CHAPTER 6

EXPERIMENTAL STUDY FOR A BATTERY MODULE

6.1. Experimental Setup

The operating temperature limits can be exceeded if a cooling system is not introduced to battery system. Hence, a cooling system is crucial to increase performance of a battery cell and to overcome safety issues in battery systems. Thermal characteristics of lithium-ion pouch cell have been studied in the previous chapter. In the real life, great number of battery cells are connected with each other in serial or parallel configurations and are used for different purposes such as in electric vehicles, in electronic devices, in scooters and so on. Here, a battery module is created by connecting three battery cells in serial and various cooling methods have been implemented and results are tabulated.

All the experiments are conducted at 1C charge rate and 1C-3C discharge rate. The T and V values are measured via K-type thermocouples during charging and discharging process. One thermocouple is positioned near the positive tab of the battery cell to measure temperature change during the experiments (Figure 6.1). Four thermocouples are used to measure the coolant (air and water) temperatures at the inlet and the outlet section of the cooling system. Moreover, one thermocouple is utilized to record ambient temperature.

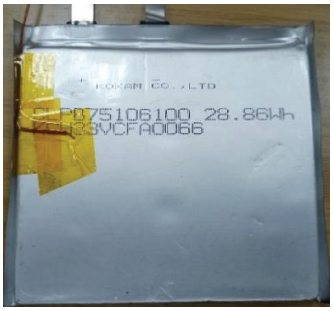

Figure 6.1. The location of thermocouple on the surface of a pouch cell

The cooling channels are manufactured from copper (Figure 6.2). The surface of battery cells and cooling plates are in contact with each other. In order to reduce contact resistances between the heat transfer surfaces, a thermal paste/grease has a thermal conductivity of 5.3 W/m.K and a thermal pad has a thermal conductivity of 3.6 W/m.K, are used solely. There are totally two cooling channels and three battery cells in the battery system.

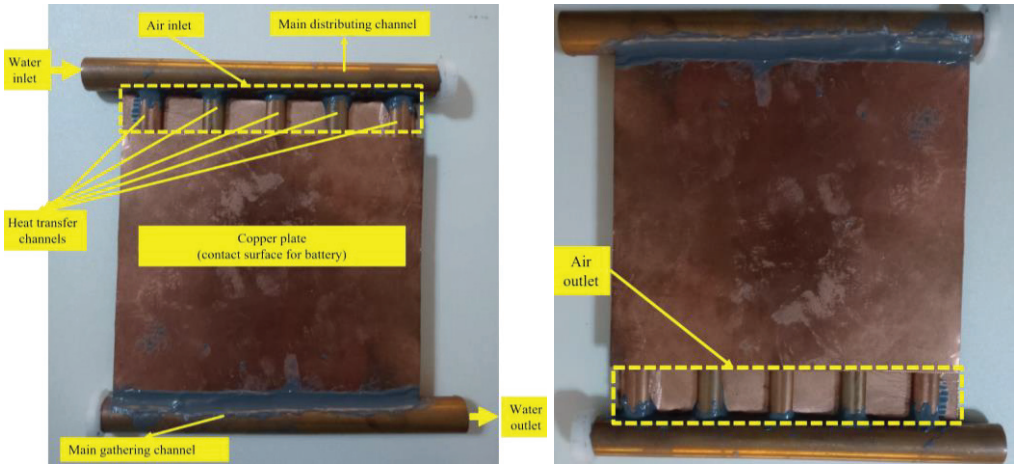

(a) (b)

Figure 6.2. View of the cooling channel from (a) front side and (b) back side

The cooling channels and batteries are placed in an order to allow air flow without any disturbances (Figure 6.3). A distributing channel and a gathering channel are utilized to distribute and collect the coolant liquid, respectively. Five elliptic heat transfer channels are placed between the distributing channel and gathering channel. The heat transfer channels with an elliptical cross section enables to liquid flow between distributing channel and gathering channel. The contact area between the heat transfer channels and plates is increased thanks to elliptical form. Hence, heat transfer is enhanced. Another advantage of elliptical form of heat transfer channels is decrement in the area occupied by thermal management system. Air enters the cooling channel from upper part of the cooling plate and leaving from the lower part of the cooling plate and is flowing between the elliptic heat transfer channels.

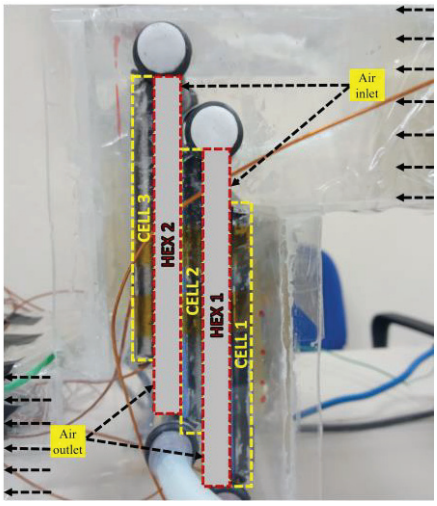

Figure 6.3. The alignment of battery cells and heat exchangers

The cooling system is shown in Figure 6.4. The cooling channels and batteries are placed in a plexiglass to hold them together and a battery system is created. Battery management system (BMS) are connected to batteries by using cables and crocodiles. Air and liquid are supplied to the system via silicon pipes and an air manifold, respectively. Three honeycombs are located inside of the duct to regulate air flow. The cooling liquid with a desired temperature is supplied to the system via a water bath. A fan with a capacity of 0.042 m^3/s is used to supply air to the system. The gaps between the connection points of the battery tabs are closed by using fiberglass to prevent air leakage from the battery system.

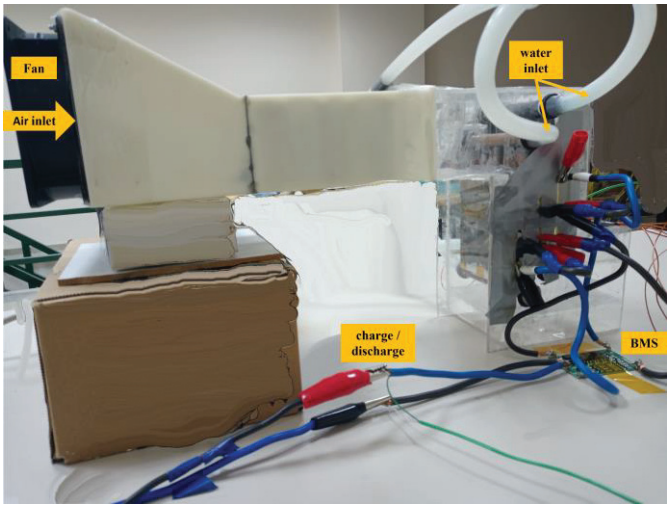

Figure 6.4. Cooling system with manifold design

The experimental setup is schematically shown in Figure 6.5. To sum up, all system consisting of the following components: water bath, needle valve, flowmeter, datalogger, charger, discharger, axial fan, HEXs, lithium-ion pouch cells and many thermocouples. The needle valve and the flowmeter are utilized to regulate liquid flow and measure to flow rate of the coolant, respectively. A circulating water bath and an axial fan are used to supply water and air to the cooling system, respectively. In the air manifold, three honeycombs are used to regulate air flow through the duct. The charging and discharging of the battery cells are carried out via power supply and electronic load, respectively. Thermocouples are utilized to measure temperature and voltage values. A set of thermocouples which are located at the inlet and outlet section of the cooling system measure the coolants temperatures. All the measured temperature and voltage values are recorded by data logger. The capacity of the cooling system is determined via measured values.

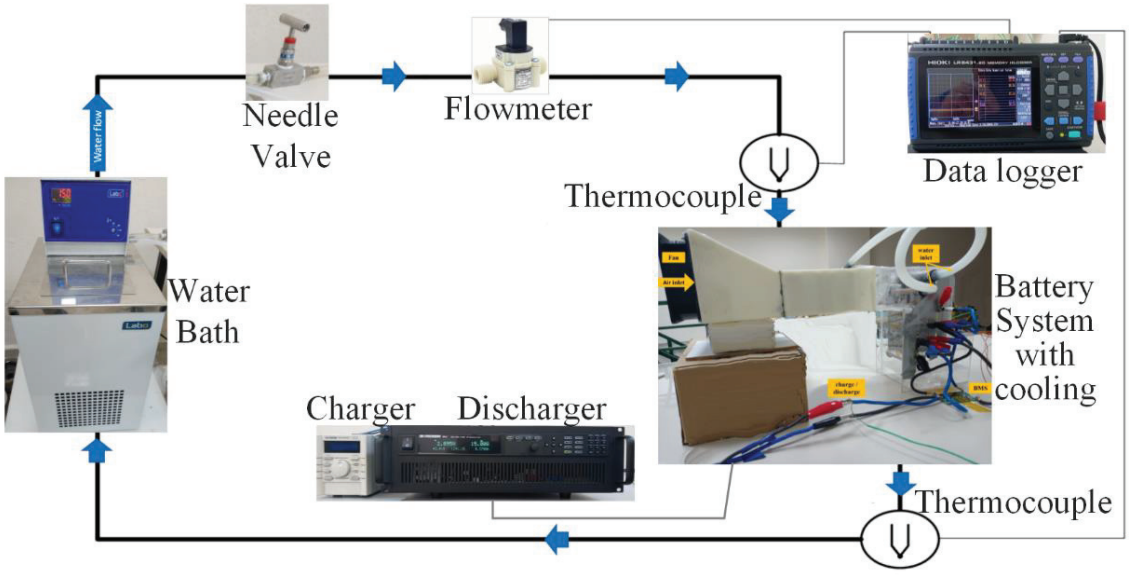

Figure 6.5. Schematics of the experimental setup

CHAPTER 7

RESULTS AND DISCUSSION

In the experimental study, a lithium-ion pouch cell (Kokam, SLPB75106100) is utilized. A battery module is created by connecting three lithium-ion pouch cells in serial. All the experiments are carried out at 1C rate charging and only heat transfer mechanism is natural convection. After the cells reaching to the thermal equilibrium after charging, 1C and 3C rates were used for discharging. The main objective of the thesis is to ensure that battery module working in the best temperature range. Various cooling methods are imposed to battery cells to achieve the goal of the Thesis.

7.1. Charge

The charging process occurs in two steps: constant current (CC) and constant voltage (CV). There is only natural convection during charging of battery cells. The change of temperature and voltage values during charging with respect to state of charge (SOC) is shown in Figure 7.1. According to Figure 7.1, the temperature remains in optimum range when environmental temperature is 23ºC. The charging start with CC mode and the temperature of the battery cells increases during this mode. A temperature drop in a short time range interval in middle of the CC mode is observed and this situation can be related to chemical reactions occurring inside the battery cell. The temperature of the battery cells is started to decrease when the charging mode change from CC to CV. The reason behind that situation is the reduction in supplied current to the batteries. According to Figure 7.1, there is only 4 °C increment in temperature during the 1C charge rate, so it is not needed to use cooling systems at 1C charge rate. There is a homogeneous temperature distribution between the cells in the module and the maximum temperature difference between the cell is 0.5°C.

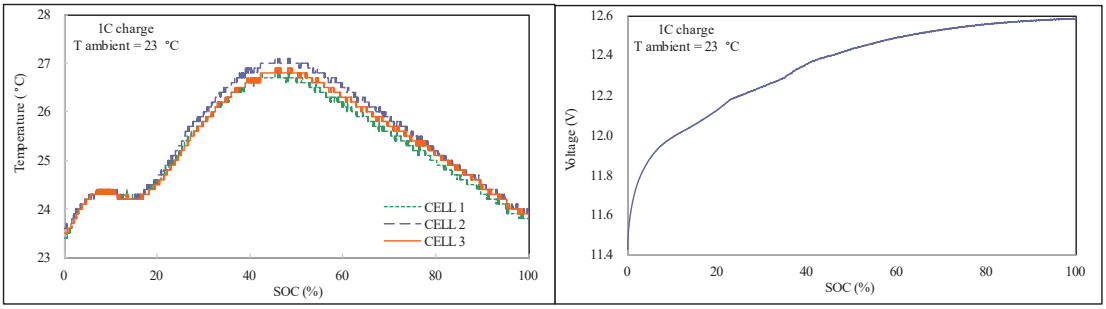

(a) (b)

Figure 7.1. The change in (a) temperature (b) voltage of 3S battery cells during 1C charge

7.2. Discharge: Constant Current

Discharging of battery cells carried out in CC mode. The change of temperature and voltage values with respect to dept of discharge (DOD) at 1C discharge rate are shown in Figure 7.2(a) and (b). The cells are subjected to cooling under natural convection during discharging process. According to the Figure 7.2(a), the temperature of the cells remain within the optimum operating range when ambient temperature is 23°C. There is only 0.5°C temperature difference between the cells during 1C discharge rate. The small fluctuations in the temperature values can be related to environmental factors like heat dissipated by equipments. There is a slight temperature differences between the Cell 1 and the others. These difference can be related to misalignment of the experimental setup. The change in voltage with respect to DOD is given in Figure 7.2(b) and it shows a sharp decrease at the end of the discharge. Discharge of the battery module is completed in 3431 seconds and the capacity of the battery module is defined as 7.147 Ah at 1C discharge rate.

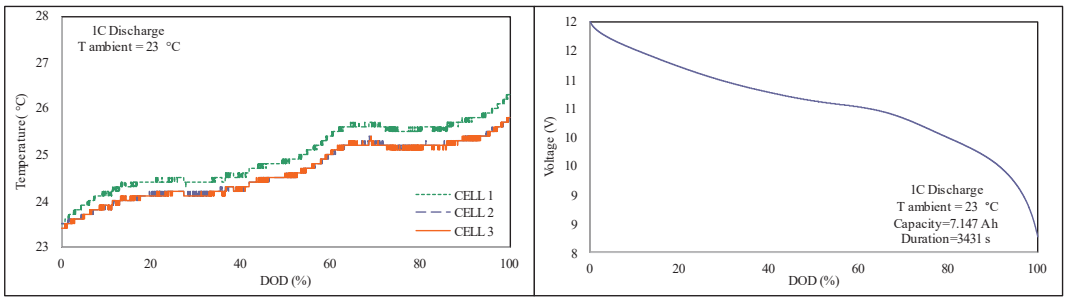

(a) (b)

Figure 7.2. The change in (a) temperature (b) voltage of 3S battery cells during 1C discharge

7.2.1. Air Cooling

The battery module is cooled by air, water, and hybrid systems. Firstly, air cooling introduced to the battery module at 3C discharge rate. According to the Figure 7.3(a), the highest temperature values are observed in Cell 3 and the temperature reaches 33.7°C at the end of the discharge. Also, the maximum temperature difference between the cells is only 1.5°C. The non homogeneous distribution of the air flow between the batteries might be the reason for the temperature difference. The cooling capacity of air is determined as 5 W. The change in voltage values with respect to DOD are given in Figure 7.3(b). In the beginnig and at the end of the discharging process there is a sharp decrease in voltage values. The voltage curve in water and hybrid cooling follow a similar trend to that in air cooling at 3C discharge rate.

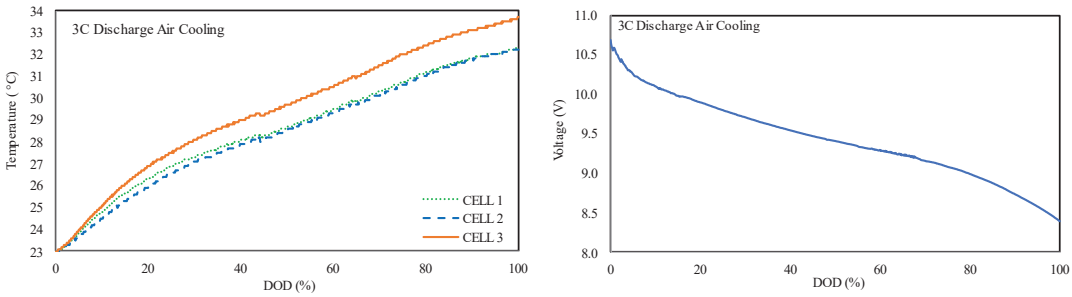

(a) (b)

Figure 7.3. The change in (a) temperature and (b) voltage of 3S battery cells during 3C discharge with air cooling

7.2.2. Water Cooling

Secondly, water cooling is introduced to the battery module. The temperature of the coolant liquid is defined as 23°C which has the same value as the ambient. As it shown in Figure 7.4, almost 7% reduction in the maximum temperature is obtained in water cooling system when compared to air cooling system. The temperature values in Cell 1 and Cell 3 are very close to each other and there is only 0.7°C difference between them. However, there is almost 4°C temperature difference between the Cell 2 and the others. This situation can be explained by the position of the Cell 2. It is located in the middle of the cooling system, and it is cooled from both sides because of the symmetric shape. Therefore, as the number of cells increases in a module cell except the ones located near the entrance and exit would yield a similar temperature trend as in Cell 2. The cooling capacity of water system is defined as 15 W.

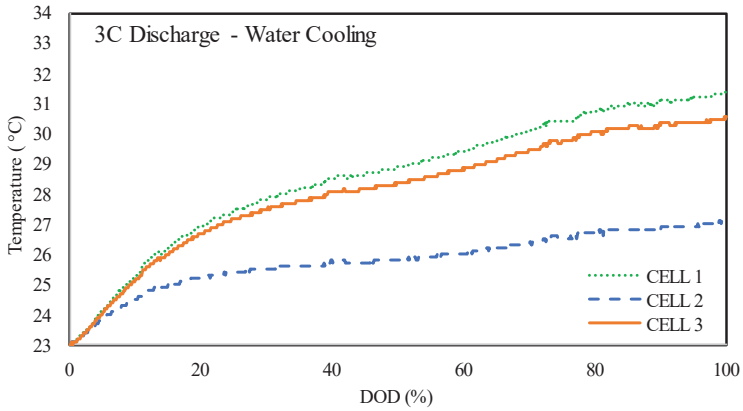

Figure 7.4. The change in temperature of 3S battery cells during 3C discharge: water cooling

7.2.3. Hybrid Cooling

Finally, the battery cells are cooled by hybrid system. In the hybrid system, air and liquid cooling are used simultaneously. According to the Figure 7.5, each cell

temperature is kept below 29°C at hybrid cooling. In addition, the maximum temperature difference between the cells is 2.7°C and it is almost 30% lower than that of liquid cooling. The temperature trend in Figure 7.5 shows that the thermal management of the battery module is achieved via hybrid cooling for 3C discharge rate at an ambient temperature of 23°C.

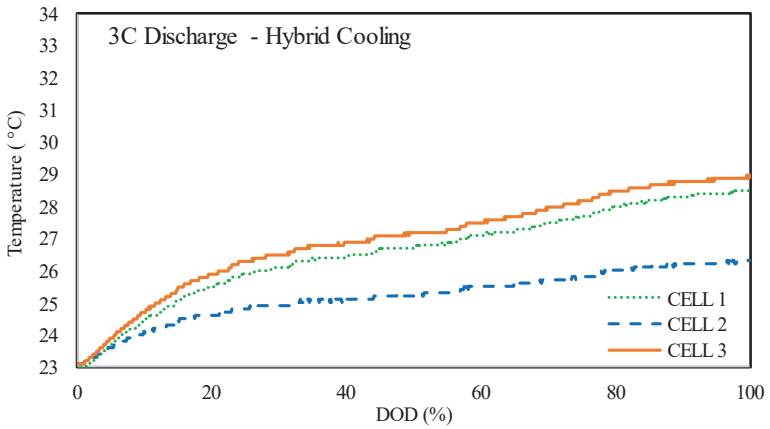

Figure 7.5. The change in temperature of 3S battery cells during 3C discharge: hybrid cooling

7.2.4. Comparison of the Cooling Systems

Air and water cooling are introduced to the battery module solely or simultaneously. In Figure 7.6, the results of Cell 2 at 3C dicharge rate is shown. In the comparison of cooling methods Cell 2 is selected because of position in the battery module. A battery pack in an electric vehicle is consists of many cells and most of the cells in the battery pack behaves like Cell 2. According to the Figure 7.6, the highest temperature values are observed in air cooling. Almost 2.5 % improvement in the maximum temperature is achieved by hybrid cooling when compared to water cooling. The temperature of battery cells are in operating limits in air cooling but the temperature trend show that the air cooling will be insufficient in extreme conditions such as aggressive driving cycles, high ambient temperatures, high discharge rate and so on.

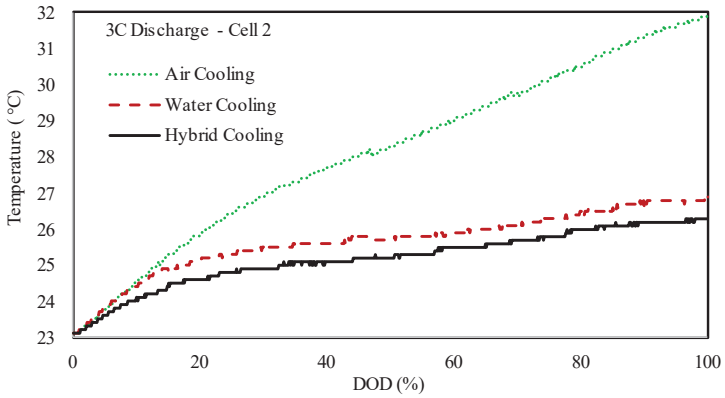

Figure 7.6. The change in temperature of Cell 2 under various cooling methods during 3C discharge

The comparison between the cooling systems is made in cell level and the results are tabulated in Table 7.1. According to the Table 7.1, the temperature of the battery cells is kept in operating limits by each cooling systems. The highest and lowest temperature values in battery cell are recorded for air and hybrid cooling, respectively. The temperature difference between the cells is minimum for air cooling and maximum for water cooling.

Table 7.1. Summary of the results for a battery module

	$T\ max$(°C)			$T\ rise$(°C)			$\Delta T\ max$(°C)		
3C Discharge	Air Cooling	Water Cooling	Hybrid Cooling	Air Cooling	Water Cooling	Hybrid Cooling	Air Cooling	Water Cooling	Hybrid Cooling
Cell 1	32.3	31.3	28.5	9.3	8.3	5.6			
Cell 2	32.2	27.1	26.3	9.2	4.1	3.2	0.5	4.2	2.7
Cell 3	33.7	30.6	29	10.7	7.6	5.9			

7.3. Discharge: Step Function

There will be not continuous load on the battery cells during the operation and the heat generation profile will be changed with respect to the usage of electric vehicle. A

step function is introduced to the battery module to determine the cooling capacity of air system during operation. In the step function, the battery module is subjected to a discharge at a rate of 3C for 270 s and then discharged at a rate of 1C for 810 s. This process continues until the discharging process is completed.

7.3.1. Air Cooling

Figure 7.7 shows the temperature and voltage profiles of the batteries during the operation under air cooling. According to Figure 7.7(a), air cooling is kept cell temperatures below 30°C when various loading imposed to battery module. Moreover, the maximum temperature difference is kept below 3°C. The highest temperature values occuring at Cell 1 and it is almost 30°C. The discharging process is completed in 2354 seconds and the capacity of the battery is 7.153 Ah.

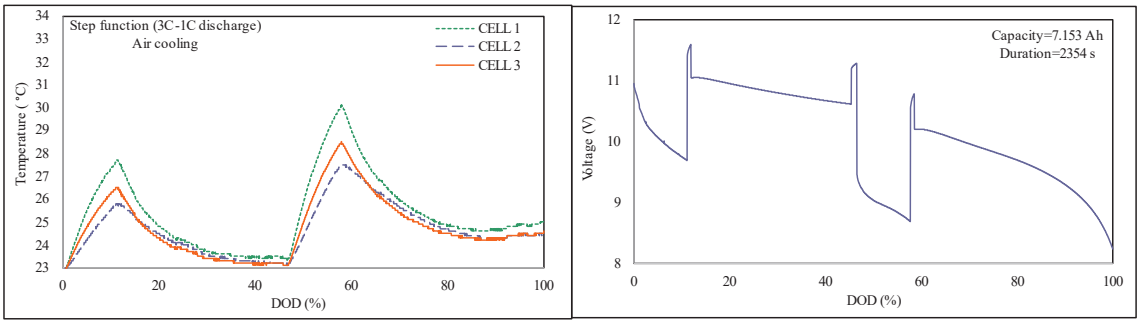

(a) (b)

Figure 7.7. The change in (a) temperature and (b) voltage values of battery cells in battery module during air cooling under step function

CHAPTER 8

CONCLUSIONS

Thesis is mainly based on the cooling of electric vehicle battery cells. There are various methods used in the cooling of the battery cells such as air cooling, liquid cooling, phase change cooling and etc. Microchannel heat sinks are one of the possible solutions for the cooling of the battery cells. There are a few studies/applications related to MCHS cooling in electric vehicle batteries. However, the popularity of electric vehicles is increase in the worldwide and this situation will contribute to development of electric vehicle industry and utilizing of MCHS in the cooling of electric vehicle batteries. Therefore, one of the subjects of the thesis is to uncover using micro heat exchangers in the cooling of battery cells. Therefore, experimental, and numerical studies in the literature about the heat transfer and flow characteristic in micro scale heat exchangers are investigated in detail to understand the feasibility of microchannel heat sinks for the application in battery thermal management system.

According to literature, the characteristic of heat and fluid flow in MCHS are not resolved exactly and there is not consistency between the results of published documents. In order to understand heat and flow characteristics and make contribution to studies at micro scale levels, we should be aware of the following arguments.

- There is no new physical phenomenon in microscale literature. Only difference between the macroscale is that the effect of surface roughness, EDL, axial heat conduction, aspect ratio, rarefaction effect, viscous dissipation, and so forth, are negligibly small in macroscales.

- Experimental and numerical research is suggested to be conducted simultaneously to increase the accuracy of the results. Viscous dissipation, axial heat conduction, and rarefaction (for gaseous flow) effects should be considered while evaluating heat transfer and fluid flow in MCHS.

- Continuum assumption in microscale is validated for liquid flow and generally problematic for gaseous flow. If Kn number is lower than 0.001, the gaseous flow can also be treated as continuum.

- Viscous dissipation can increase or decrease heat transfer depending on Br number (heating or cooling). The friction factor reduces due to a decrease in apparent viscosity as temperature increases in the heating case.

- The effect of axial heat conduction in MCHS becomes negligible when Pe < 100.

- The effect of surface roughness on heat transfer is generally insignificant; however, the change in friction factor with surface roughness is remarkable according to the literature. Surface roughness effect on the friction factor and heat transfer is generally pronounced with rarefaction effect for gaseous flow, and it becomes significant at low Kn number values.

- EDL affects liquid flow in microchannels and creates resistance to the fluid flow at the vicinity of the solid wall, that is, rise in apparent viscosity. This increases pumping power requirements in MCHS.

-Overall, geometrical parameters should be defined as certain as possible and manufacturing constraints needed to be defined clearly before the experiments. When comparing the results of experimental studies, all the assumptions should agree with the methodology. The literature shows that there is disagreement in MCHS literature, and the physics of fluid flow should be focused more. To increase consistency between the literature and to understand the physical phenomena at microscale accurately, experimental and numerical studies should consider all physical phenomena in their studies and state all assumptions and criteria to justify the reason of why some phenomena are neglected if applicable. Thus, would enable the audience to compare the microscale heat transfer literature and realize the effect of each physical phenomena on heat transfer and pressure drop accurately.

In addition to the review on MCHS, a numerical study which is mainly based on heat transfer enhancement in MCHS is conducted by inserting micro pin fins and nanofluids. The numerical study is conducted via COMSOL software and increase in pressure drop and heat transfer rate in microchannel heat sinks are determined. According to the numerical results the heat transfer rate in microchannels is enhanced by the extension of the heat transfer surfaces. However, the pressure drops in the microchannels also increase with the rising of heat transfer surface area. As a result, using microchannel heat sinks in battery cooling is not feasible because of higher pressure drop values. Thus, it is decided to design a heat exchanger in conventional length scales and introduce to battery cells.

In the study of battery cooling, various approaches have been used. Firstly, the study conducts on a silicone heater system to understand the thermal behaviour of the battery cells. And, then the experimental studies are conducted in a single lithium-ion battery cell to visualize temperature distribution on surface of the battery cell. Silicone heater system is tested under various heating loads. It is aimed to estimate thermal behaviours of battery cell at various discharge rate by using various heating loads in the silicone heater system. The silicone heater system can be good approximation to understand the thermal behaviour of the battery cell and it might be an economical way of conducting experimental studies. Furthermore, the safety problems arise in battery cells during experimental studies such as thermal runaway, fire of cells, short circuit and so on, can be eliminated in the silicone heater system. After that, experimental studies are carried out using a single lithium-ion battery to characterize thermal behaviour of the battery cell. The results show that heat generation is dense near the tabs, and it changes with respect to the charge/discharge rate.

Lastly, the experimental studies are carried out in a battery module. Battery packs/modules are created by connecting many cells in serial or parallel configurations and they are used in electric vehicles as a power source. Here, a battery module, consists of three pouch cells connected in series, is cooled by implementing various cooling methods. According to the results, all the cooling systems are met the requirements of battery system at 3C discharge rate when the ambient temperature is 23°C. In the water cooling, the lowest temperature values are recorded in the middle cell because of the symmetric shape (it cooled from both sides). The most uniform temperature distribution and the lowest temperature values are observed in the air cooling and the hybrid cooling, respectively. The temperature of battery cells remains in the operating limits during air cooling; however, the temperature profile shows that the air cooling will be failed in extreme conditions such as aggressive driving cycles, high ambient temperatures, high discharge rates and so on. The result proves that air cooling will be the best solution for low capacity cells. In the hybrid system, the battery module is cooled by air, liquid, or the hybridization between them. The cooling system can be selected with respect to the operating conditions. Hence, an optional energy efficient cooling system is developed by the hybrid cooling. In order to simulate the performance of air cooling during the operation of electric vehicles, a step function is created. In the step function, discharging process is carried out in the following sequence: discharge at the 3C rate for 270 seconds

and discharge at the 1C rate for 810 seconds. The result shows that the cell temperatures are kept below 30°C during step function when the ambient temperature is 23°C.

8.1. Further Studies

The silicone heater system can be improved by defining new parameters. A time dependent code can be developed with respect to the heat generation profile in a battery cell and it is embedded into the power supply to introduce a predefined heating load for silicon heater.

The battery cell can be modeled via a computational fluid dynamics software and the experimental model can be validated with respect to the numerical model. In addition, the numerical model can be used to develop the existing designs (the heat exchanger and the battery system used in the thesis)

REFERENCES

Adewumi, O.O.; Bello-Ochende, T.; Meyer, J.P. Comparison between the thermal performance of single and two-layer microchannels inserted with micro pin fins. *Proceedings of the 15th Heat Transfer Conference*, Kyoto, Japan, August 10-15, 2014.

Adewumi, O.O.; Bello-Ochende, T.; Meyer, J.P. Constructual design of combined microchannel and micro pin fins for electronic cooling. *Int. J. Heat Mass Transfer*. 2013, 66, 315-323.

Affanni A. et al. Battery Choice and Management for New-Generation Electric Vehicles. *IEEE Transactions on Industrial Electronics*. 2005, 52, 1343-1349.

Al-Hallaj, S.; Selman, J. R. Thermal modeling of secondary lithium batteries for electric vehicle/hybrid electric vehicle applications. *J. Power Sources*. 2002, 110, 341-348.

Alshaer, W.G.; Nada, S.A.; Rady, M.A.; Del Barrio, E.P.; Sommier, A. Thermal management of electronic devices using carbon foam and PCM/nano-composite. *Int. J. Thermal Sciences*. 2015, 89, 79-86.

Al-Zareer, M.; Dincer, I.; Rosen, M. A. A review of novel thermal management systems for batteries. *Int. J. Energy Res*. 2018, 42, 3182–3205.

Anoop, K.B.; Sundararajan, T.; Das, S.K. Effect of particle size on the convective heat transfer in nanofluid in the developing region. *Int. J. Heat and Mass Transfer*. 2009, 52, 2189-2195.

Arkilic, E. B.; Schmidt, M. A.; Breuer, K. S. Gaseous Flow in Long Microchannel. *J. MEMS.* 1997, 6, 167-178.

Arora, S.; Kapoor, A. Experimental Study of Heat Generation Rate during Discharge of LiFePO4 Pouch Cells of Different Nominal Capacities and Thickness. *Batteries*. 2019, 5, 1-22.

Arora, S.; Shen, W.; Kapoor, A. Neural network based computational model for estimation of heat generation in LiFePO4 pouch cells of different nominal capacities. *Computers and Chemical Engineering*. 2017, 101, 81-94.

Bandhauer, T. M.; Garimella, S.; Fuller, T. F. A Critical Review of Thermal Issues in Lithium-Ion Batteries, *J. Electrochemical Society*. 2011, 158, R1-R25.

Bandhauer, T. M.; Garimella, S. Passive, internal thermal management system for batteries using microscale liquidevapor phase change, *Applied Thermal Engineering*. 2013, 61, 756-769.

Barisik, M.; Yazicioglu, A. G.; Çetin B.; Kakaç, S. Analytical solution of thermally developing microtube heat transfer including axial conduction, viscous dissipation, and rarefaction effects. *Int. Communications in Heat and Mass Transfer*. 2015, 67, 81-88.

Bazinski, S. J.; Wang, X.; Predicting heat generation in a lithium-ion pouch cell through thermography and the lumped capacitance model. *J. Power Sources*. 2016, 305, 97-105.

Bejan, A., Lorente, S. Design with Constructal Theory; Hoboken, NJ, USA: J. Wiley and Sons, Inc. Press, 2008.

Bello-Ochende, T.; Meyer, J.P.; Ighalo, F.U. Combined numerical optimization and constructal theory for the design of microchannel heat sinks. *Numerical Heat Transfer, Part A*. 2010, 58, 882-899.

Bernardi, D.; Pawlikowski, E.; Newman, J. A general energy balance for battery systems. *J. Electrochem. Soc*. 1984, 132, 5–12.

Bhattacharjee, G.S.; Grosshandler, W.L. The formation of wall jet near a high temperature wall under microgravity environment. *American Society of Mechanical Engineers, Heat Transfer Division.* 1988, 96, 711-716.

Buongiomo J. et al. A benchmark study on the thermal conductivity of nanofluids. *J. Applied Physics*. 2009, 106, 094312.

Chandrasekar, M.; Suresh, S.; Chandra Bose, A. Experimental investigations and theoretical determination of thermal conductivity and viscosity of Al_2O_3/water nanofluid. *Experimental Thermal and Fluid Science*. 2010, 34, 210-216.

Chandrasekar, M.; Suresh, S.; Bose, A. C. Experimental studies on heat transfer and friction factor characteristics of Al_2O_3/water nanofluid in a circular pipe under transition flow with wire coil inserts. *Heat Transfer Engineering*. 2011, 32(6), 485–496.

Chen, C. H. Slip-flow heat transfer in a microchannel with viscous dissipation. *Heat Mass Transfer*. 2006, 42, 853–860.

Chen, D.; Jiang, J.; Kim, G.H.; Yang, C.; Pesaran, A. Comparison of different cooling methods for lithium ion battery cells. *Applied Thermal Engineering*. 2016, 94, 846–854.

Chen, K.; Unsworth, G.; Li, X. Measurements of heat generation in prismatic Li-ion batteries. *J.Power Sources*. 2014, 261, 28-37.

Chen, Y.; Evans, J. W. Thermal analysis of lithium polymer electrolyte batteries by a two-dimensional model-thermal behaviour and design optimization. *Electrochimica Acta*. 1994, 39, 517-526.

Chen, Y.; Zang, C.; Shi, M.; Peterson, G. P. Role of surface roughness characterized by fractal geometry on laminar flow in microchannels. *Physical Review E.* 2009, 80, 026301(1-7).

Choi, S.U.S.; Eastman, J.A. Enhancing thermal conductivity of fluids with nanoparticles. In *Developments and Applications of Non- Newtonian Flows; DA Siginer, HP Wang, Am. Soc. Mech. Eng*., 1995.

Choi, S.U.S.; Zhang, Z.G.; Yu, W.; Lockwood, F.E.; Grulke, E.A. Anomalous thermal conductivity enhancement in nanotube suspensions. *Applied Physics Letters*. 2001, 79(14), 2252-2254.

Chung, Y.; Kim, M.S. Thermal analysis and pack level design of battery thermal management system with liquid cooling for electric vehicles. *Energy Convers. Manage*. 2019, 196, 105-116.

Cole, K. D.; Çetin, B. The effect of axial conduction on heat transfer in a liquid microchannel flow. *Int. J. Heat Mass Transfer*. 2011, 54, 2542-2549.

COMSOL Multiphysics, version 5.0, COMSOL Inc., Burlington, MA: 2014.

Coşkun T.; Çetkin, E. Heat Transfer Enhancement in a Microchannel Heat Sink: Nanofluids and/or Micro Pin Fins. *J. Heat Transfer Engineering*. 2019, 41(21), 1818-1828.

Croce G.; D'Agaro, P. Numerical simulation of roughness effect on microchannel heat transfer and pressure drop in laminar flow. *J. Applied Physics*. 2005, 38,1518-1530.

Çetin, B.; Yazicioglu, A. G.; Kakaç, S. Fluid flow in microtubes with axial conduction including rarefaction and viscous dissipation. *Int. Communications in Heat and Mass Transfer*. 2008, 35, 535-544.

Dai, B.; Li, M.; Ma, Y. Effect of surface roughness on liquid friction and transition characteristics in micro- and mini-channels. *Applied Thermal Engineering*. 2014, 67, 283-293.

Dan, D.; Yao, C.; Zhang, Y.; Zhang, H.; Zeng, Z.; Xu, X. Dynamic thermal behavior of micro heat pipe array-air cooling battery thermal management system based on thermal network model. *Applied Therm Engineering*. 2019, 162.

Dang, T.; Teng, J. T. Comparisons of the heat transfer and pressure drop of the microchannel and minichannel heat exchangers. *J. Heat Mass Transfer*. 2011, 47, 1311-1322.

Das, S. K.; Choi, S. U. S.; Patel, H. E. Heat transfer in nanofluids—A review. *Heat Transfer Engineering*. 2006, 27(10), 3-19.

Das, S.K.; Putra, N.; Thiesen, P.; Roetzel, W. Temperature Dependence of Thermal Conductivity Enhancement for Nanofluids. *J. Heat Transfer*. 2003, 125, 567-574.

Dewan, A.; Srivastava, P. A review of heat transfer enhancement through flow disruption in a microchannel. *J. Thermal Science*. 2015, 24(3), 203-214.

Fani, B.; Kalteh, M.; Abbassi, A. Investigating the effect of Brownian motion and viscous dissipation on the nanofluid heat transfer in a trapezoidal microchannel heat sink. *Advanced Powder Technology*. 2015, 26, 83-90.

Fathabadi, H. A novel design including cooling media for Lithium-ion batteries pack used in hybrid and electric vehicles. *J. Power Sources*. 2014, 245, 495-500.

Feng, X.; Zheng, S.; Ren, D.; He, X.; Wang, L.; Cui, H.; Liu, X.; Jin, C.; Zhang, F.; Xu, C.; Hsu, H.; Gao, S.; Chen, T.; Li, Y.; Wang, T.; Wang, H.; Li, M.; Ouyang M. Investigating the thermal runaway mechanisms of lithium-ion batteries based on thermal analysis database. *Applied Energy*. 2019, 53-64.

Gad-el-Hak, M. The Fluid Mechanics of Microdevices-The Freeman Scholar Lecture. *J. Fluids Engineering*. 1999, 121, 5-33.

Garimella S. V., Singhal, V. Single-Phase Flow and Heat Transport and Pumping Considerations in Microchannel Heat Sinks. *Heat Transfer Engineering*. 2004, 25(1), 15-25.

Ghanbarpour, M.; Bitaraf Haghigi, E.; Khodabandeh, R. Thermal properties and rheological behavior of water based Al2O3 nanofluid as a heat transfer fluid. *Experimental Thermal and Fluid Science*. 2014, 53, 227-235.

Goutam, S.; Nikolian, A.; Jaguemont, J.; Smekens, J.; Omar, N.; Bossche, P. V. D.; Mierlo, J.V. Three-dimensional electro-thermal model of li-ion pouch cell: Analysis and comparison of cell design factors and model assumptions. *Applied Thermal Engineering*. 2017, 126, 796–808.

Guo, Z. Y.; Li, Z. X. Size effect on single-phase channel flow and heat transfer at microscale. *International Journal of Heat and Fluid Flow*. 2003, 24, 284-298.

Han, X.; Lu, L.; Zheng, Y.; Feng, X.; Li, Z.; Li, J.; Ouyang, M. A review on the key issues of the lithium ion battery degradation among the whole life cycle. *eTransportation*. 2019, 1, 100005(1-21).

Harms, T. M.; Kazmierczak, M. J.; Gerner, F. M. Developing convective heat transfer in deep rectangular microchannels. *Int. J. Heat Fluid Flow*. 1999, 20, 149-157.

Herwig, H.; Hausner, O. Critical view on new results in micro-fluid mechanics: an example. *Int. J. Heat and Mass Transfer*. 2003, 46, 935-937.

Herwig, H.; Mahulikar, S. P. Variable property effects in single-phase incompressible flows through microchannels. *Int. J. Thermal Sciences*. 2006, 45, 977-981.

Hetsroni, G.; Mosyak, A.; Pogrebnyak E.; Yarin, L. P. Fluid flow in micro-channels. *Int. J. Heat and Mass Transfer*. 2005, 48, 1982-1998.

Horie, H.; Abe, T.; Kinoshita, T.; Shimoida, Y. A Study on an Advanced Lithium-ion Battery System for EVs. *The World Electric Vehicle J*. 2008, 2, 25-31.

Hosseinzadeh, E.; Marco, J.; Jennings, P. Electrochemical-Thermal Modelling and Optimisation of Lithium-Ion Battery Design Parameters Using Analysis of Variance. *Energies*. 2017, 10, 1278(1-22).

Huang, C. Y.; Wu, C. M.; Chen, Y. N.; Liou, T. M.The experimental investigation of axial heat conduction effect on the heat transfer analysis in microchannel flow. *Int. J. Heat Mass Transfer*. 2014, 70, 169-173.

Hunter, R. J. *Zeta potential in colloid Science: principles and applications*; Academic Press, 1981.

Huo, Y.; Rao, Z.; Liu, X., Zhao, J. Investigation of power battery thermal management by using mini-channel cold plate. *Energy Conversion and Management*. 2015, 89, 387–395.

Incropera, F.P.; Dewitt, D.P.*Fundementals of Heat and Mass Transfer*; 2nd Edition, 1985.

Javani, N.; Dincer, I.; Naterer, G.F.; Rohrauer, G.L. Modeling of passive thermal management for electric vehicle battery packs with PCM between cells. *Applied Thermal Engineering*. 2014, 73, 307-316.

Jayaraj, S.; Kang, S.; Suh, Y. K. A Review on the Analysis and Experiment of Fluid Flow and Mixing in Micro-Channels. *J. Mechanical Science and Technology*. 2007, 21, 536-548.

Kakaç, S.; Vasiliev, L. L.; Bayazitoglu, Y.; Yener, Y. *Microscale Heat Transfer, Fundamentals and Applications*; *NATO Science Series, II. Mathematics, Physics and Chemistry*, vol. 193; Springer Press, 2005.

Kakaç, S.; Yazicioglu, A. G.; Gözükara, A. C. Effect of variable thermal conductivity and viscosity on single phase convective heat transfer in slip flow. *Heat Mass Transfer*. 2011, 47, 879-891.

Kalyoncu, G.; Barisik, M. The extended Graetz problem for micro-slit geometries; analytical coupling of rarefaction, axial conduction and viscous dissipation. *Int. J. Thermal Sciences*. 2016, 110, 261-269.

Kandlikar, S. G. History, Advances, and Challenges in Liquid Flow and Flow Boiling Heat Transfer in Microchannels: A Critical Review. *J. Heat Transfer*. 2012, 134, 034001-1,15.

Kandlikar, S. G.; Garimella, S.; Li, D.; Colin, S.; King, M. R. *Heat Transfer and Fluid Flow in Minichannels and Microchannels*; Elsevier Press, 2006.

Kandlikar, S. G.; Grande, W. J. Evolution of microchannel flow passages: thermo-hydraulic performance and fabrication technology. *Proceedings of the ASME international mechanical engineering congress exposition*, New Orleans, Louisiana, 2002.

Kandlikar, S. G.; Joshi, S.; Tian, S. Effect of Surface Roughness on Heat Transfer and Fluid Flow Characteristics at Low Reynolds Numbers in Small Diameter Tubes. *Heat Transfer Engineering*. 2003, 24(3), 4-16.

Karimi, G.; Li, X.; Thermal management of lithium-ion batteries for electric vehicles. *Int. J. Energy Res.* 2013, 37, 13-24.

Karimzadehkhouei M. et al. Experimental and numerical investigation of inlet temperature effect on convective heat transfer of c-Al2O3/water nanofluid flows in microtubes. *Heat Transfer Eng*ineering. 2018, 40, 738–752.

Keyser, M.; Pesaran, A.; Li, Q. et al. Enabling fast charging: Battery thermal considerations, *J. Power Sources*. 2017, 367, 228-236.

Khan, W. A.; Culham, J. R.; Yovanovich, M. M. Performance of shrouded pin-fin heat sinks for electronic cooling. *J. Thermophysics Heat Transfer*. 2006, 20(3), 408–414.

Kim, D. K.; Kim, S. J. Averaging approach for microchannel heat sinks subject to the uniform wall temperature condition. *International Journal of Heat and Mass Transfer*. 2006, 49, 695-706.

Kim, U. S.; Shin, C. B.; Kim, C. S. Effect of electrode configuration on the thermal behavior of a lithium-polymer battery. *J. Power Sources*. 2008, 180, 909-916.

Kleinstreuer, C.; Koo, J. Computational Analysis of Wall Roughness Effects for Liquid Flow in Micro-Conduits. *J. Fluids Engineering*. 2004, 126, 1-9.

Knight, R. W.; Hall, D. J.; Goodling, J. S.; Jaeger, R. C.; Heat sink optimization with Application to microchannels. *IEEE Transaction Componenets Hybrids Manufacturing Technology*. 1992, 15(5), 832-842.

Koo, J.; Kleinstreuer, C. Viscous dissipation effects in microtubes and microchannels. *Int. J. Heat and Mass Transfer*. 2004, 47, 3159-3169.

Kosar, A.; Mishra, C.; Peles, Y. Laminar flow across a bank of low aspect ratio micro pin fins. *J. Fluids Engineering*. 2005, 127, 419–430.

Kumaraguruparan, G.; Sornakumar, T. Development and Testing of Aluminium Micro Channel Heat Sink. *J. Thermal Science.* 2010, 19, 245-252.

Lee, P. S.; Ho, J. C.; Xue, H. Experimental study on laminar heat transfer in microchannel heat sink. *In ITherm 2002. Eighth Intersociety Conference on Thermal and Thermomechanical Phenomena in Electronic Systems* (Cat.), 2002, No.02CH37258, pp. 379-386, doi: 10.1109/ITHERM.2002.1012481.

Lin, C.; Xu, S.; Liu, J. Measurement of heat generation in a 40 Ah LiFePO4 prismatic battery using accelerating rate calorimetry. *Int. J. Hydrogen Energy*. 2018, 43, 8375-8384.

Li, D. Electro-viscous effects on pressure-driven liquid flow in microchannels. *Colloids and Surfaces A: Physicochemistry Engineering Aspects*. 2001, 195, 35-57.

Li, X.; He, F.; Zhang, G.; Huang, Q.; Zhou, D. Experiment and simulation for pouch battery with silica cooling plates andcopper mesh based air cooling thermal management system. *Applied Thermal Engineering*. 2019, 146, 866–880.

Li, Y.; Qi, F.; Guo, H.; Guo, Z.; Li, M.; Wu, W. Characteristic investigation of an electrochemical-thermal coupled model for a LiFePO4/Graphene hybrid cathode lithium-ion battery. *Case Studies in Thermal Engineering*. 2019, 13, 100387(1-11).

Li, Y.; Xie, H.Q.; Yu, W.; Li, J. Liquid cooling of tractive lithium ion batteries pack with nanofluids coolant. *J. Nanoscience Nanotechnology*. 2015, 15(4), 3206-3211.

Li, Z. X.; Du, D. X.; Guo, Z. Y. Experimental study on flow characteristics of liquid in circular microtubes. *Microscale Thermophys Engineering*. 2003, 7, 253-265.

Lin, C.; Xu, S.; Chang, G.; Liu, J. Experiment and simulation of a LiFePO4 battery pack with a passive thermal management system using composite phase change material and graphite sheets. *J. Power Sources*. 2015, 275, 742–749.

Lin, L.; Chen, Y.Y.; Zhang, X.X.; Wang, X.D. Optimization of geometry and flow rate distribution for double-layer microchannel heat sink. *Int. J. Thermal Sciences*. 2014, 78, 158-168.

Lin, M.; Wang, Q.W.; Guo, Z. Investigation on evaluation criteria of axial wall heat conduction under two classical thermal boundary conditions. *Applied Energy*. 2016, 162, 1662-1669.

Lin, T. T.; Kandlikar, S. G. A theoretical model for axial heat conduction effects during single-phase flow in microchannels. *J. Heat Transfer*. 2012, 134, 020902(1-6).

Liu, F.; Lan, F.; Chen, J. Dynamic thermal characteristics of heat pipe via segmented thermal resistance model for electric vehicle battery cooling. *J. Power Sources*. 2016, 321, 57–70.

Liu, Y.; Xu, G.; Sun, J.; Li, H. Investigation of the roughness effect on flow behavior and heat transfer characteristics in microchannels. *Int. J. Heat and Mass Transfer*. 2015, 83, 11–20.

Ma, T.; Yang, H.X.; Zhang, Y.P.; Lu, L.; Wang, X. Using phase change materials in photovoltaic systems for thermal regulation and electrical efficiency improvement: A review and outlook. *Renewable and Sustainable Energy Reviews*. 2015, 43, 1273-1284.

Mala, Gh. M.; Li, D. Flow characteristics of water in microtubes. *Int. J. Heat Fluid Flow*. 1999, 20, 142-148.

Mala, Gh. M.; Li, D.; Dale, J. D. Heat transfer and fluid flow in microchannels. *Int. J. Heat Mass Transfer*. 1997, 40(13), 3079-3088.

Maleki, H.; Deng, G.; Anani, A.; Howard, J. Thermal Stability Studies of Li-Ion Cells and Components. *J. Electrochemical Society.* 1999, 146, 3224-3229.

Maranzana, G.; Perry, I.; Maillet, D. Mini- and micro-channels: influence of axial conduction in the walls. *Int. J. Heat and Mass Transfer*. 2004, 47, 3993–4004.

Mastali M. et al. Electrochemical Modeling of Commercial LiFePO4 and Graphite Electrodes: Kinetic and Transport Properties and Their Temperature Dependence. *J. Electrochemical Society*. 2016, 163, A2803-A2816.

Mastali, M.; Foreman, E.; Modjtahedi, A.; Samadani, E.; Amirfazli, A.; Farhad, S.; Fraser, R. A.; Fowler, M. Electrochemical-thermal modeling and experimental

validation of commercial graphite/LiFePO4 pouch lithium-ion batteries. *Int. J. Thermal Sciences*. 2018, 129, 218-230.

Mehendale, S. S.; Jacobi, A. M.; Shah, R. K. Fluid flow and heat transfer at micro-and meso-scales with application to heat exchanger design. *Appl. Mech. Rev*. 2000, 53, 175–193.

Meyer, J. P.; Adio, S. A.; Sharifpur, M.; Nwosu, P. N. The Viscosity of Nanofluids: A Review of the Theoretical, Empirical, and Numerical Models. *Heat Transfer Engineering*. 2016, 37(5), 387–421.

MIT. A Guide to Understanding Battery Specifications. 2008. *http://web.mit.edu/evt/summary_battery_specifications.pdf*.

Missaggia, L. J.; Walpole, J. N.; Liau, Z. L.; Philips, R. J. Microchannel heat sinks for two-dimensional high-power-density diode laser arrays. *IEEE J. Quantum Electronics*. 1989, 25(9), 1988-1992.

Mohammadian, S. K.; He, Y. L.; Zhang, Y. Internal cooling of a lithium-ion battery using electrolyte as coolant through microchannels embedded inside the electrodes. *J. Power Sources*. 2015, 293, 458-466.

Mohammadian, S. K.; Zhang, Y. Improving wettability and preventing Li-ion batteries from thermal runaway using microchannels. *Int. J. Heat and Mass Transfer*. 2018, 118, 911-918.

Morini, G. L. Scaling Effects for Liquid Flows in Microchannels. *Heat Transfer Engineering*. 2006, 27(4), 64-73.

Morini, G. L. Single-phase convective heat transfer in microchannels: a review of experimental results. *Int. J. Thermal Sciences.* 2004, 43, 631-651.

Morini, G. L. Viscous heating in liquid flows in micro-channels. *Int. J. Heat and Mass Transfer*. 2005, 48, 3637-3647.

Morini G. L.; Spiga, M. The role of the viscous dissipation in heated microchannels. *J. Heat Transfer*. 2007, 129(3), 308-318.

Mukane, S.; Mane, P.; Gaddam, A. Performance and analysis of battery thermal management system used in electric vehicles (EVS), *Materials Today: Proceedings*. 2021, 45, 2690-2696.

Mukherjee, S.; Biswal, P.; Chakraborty, S.; Das Gupta, S. Effects of viscous dissipation during forced convection of power-law fluids in microchannels. *Int. Communications in Heat and Mass Transfer*. 2017, 89, 83-90.

Ng, E. Y. K.; Poh, S. T. CFD analysis of double-layer microchannel conjugate parallel liquid flows with electric double-layer effects. *Numerical Heat Transfer, Part A*. 2001, 40(7), 735-749.

Ng, E. Y. K.; Tan, S. T. Computation of three-dimensional developing pressure-driven liquid flow in a microchannel with edl effect. *Numerical Heat Transfer, Part A*. 2004, 45(10), 1013-1027.

Nguyen, C.T. et al. Viscosity data for Al2O3-water nanofluid-hysteresis: is heat transfer enhancement using nanofluids reliable?. *Int. J. Thermal Sciences*. 2008, 47, 103-111.

Pak, B. C.; Cho, Y. I. Hydrodynamic and heat transfer study of dispersed fluids with submicron metallic oxide. *Int. J. Experimental Heat Transfer*. 1998, 11(2), 151–170.

Pelevic N.; van der Meer, Th. H. Heat transfer and pressure drop in microchannels with random roughness. *Int. J. Thermal Sciences*. 2016, 99, 125-135.

Pan, M.; Zhong, X.; Dong, G.; Huang, P. Experimental study of the heat dissipation of battery with a manifold micro-channel heat sink. *Applied Thermal Engineering*. 2019, 163, 114330(1-13).

Peng, X. F.; Peterson, G. P. The effect of thermofluid and geometrical parameters on convection of liquids through rectangular microchannels. *Int. J. Heat Mass Transfer*. 1995, 38(4), 755-758.

Peng, X. F.; Wang, B. X.; Peterson, G. P.; Ma, H. B. Experimental investigation of heat transfer in flat plates with rectangular microchannels. *Int. J. Heat and Mass Transfer*. 1995, 38(1), 127-137.

Pesaran, A. A. Battery thermal models for hybrid vehicle simulations. *J. Power Sources*. 2002, 110, 377–382.

Pesaran, A. A.; Markel, T.; Tataria, H.S.; Howell, D. Battery Requirements for Plug-In Hybrid Electric Vehicles – Analysis and Rationale. *in the Proceeding of 23rd Electric Vehicle Symposium (EVS-23)*, Anaheim, California, December 2-5, 2007.

Petrescu, S. Comments on the optimal spacing of parallel plates cooled by forced convection. *Int. J. Heat Mass Transfer*. 1994, 37(8), 1283.

Peles, Y.; Kosar, A.; Mishra, C.; Kuo, C-J.; Schneider, B. Forced Convective Heat Transfer Across a Pin Fin Micro Heat Sink. *Int. J. Heat Mass Transfer*. 2005, 48, 3615-3627.

Pfund, D.; Rector, D.; Shekarriz, A.; Popescu, A.; Welty, J. Pressure Drop Measurements in a Microchannel. *AIChE J., Fluid Mechanics and Transport Phenomena*. 2000, 46(8), 1496-1507.

Prasher, R.S. et al. Nusselt number and friction factor of staggered arrays of low aspect ratio micropin-fins under cross flow for water as fluid. *J. Heat Transfer, Transactions of the ASME*. 2007, 129, 141-153.

Prasher, R.; Song, D.; Wang, J.; Phelan, P. Measurements of nanofluid viscosity and its implications for thermal applications. *Applied Physics Letters*. 2006, 89, 133108-3.

Qu, W.; Siu-Ho, A. Liquid Single-Phase Flow in an Array of Micro-Pin-Fins-Part I: Heat Transfer Characteristics. *J. Heat Transfer, Transactions of the ASME*, 2008, 130(12), 122402(1-11).

Rahimi, M.; Mehryar, R. Numerical study of axial heat conduction effects on the local Nusselt number at the entrance and ending regions of a circular microchannel. *Int. J. Thermal Sciences*. 2012, 59, 87-94.

Rahman, M. M. Measurements of Heat Transfer in Microchannel Heat Sinks. *Int. Communicaitons Heat Mass Transfer*. 2000, 27(4), 495-506.

Ren, L.; Li D.; Qu, W. Electro-Viscous Effects on Liquid Flow in Microchannels. *J. Colloid and Interface Science*. 2001, 233, 12-22.

Ren, L.; Qu, W.; Li, D. Interfacial electro kinetic effects on liquid flow in microchannels. *Int. J. Heat and Mass Transfer*. 2001, 44, 3125-3134.

Rosa, P.; Karayiannis, T. G.; Collins, M. W. Single-phase heat transfer in microchannels: The importance of scaling effects. *Applied Thermal Engineering*. 2009, 29, 3447-3468.

Safari, M.; Delacourt C. Mathematical modeling of lithium iron phosphate electrode: galvanostatic charge/discharge and path dependence. *J. Electrochemical Society*. 2011, 158, A63-A73.

Sahar, A. M.; Özdemir, M. R.; Fayyzh, E. M.; Wissink, J.; Mahmoud M. M.; Karayiannis, T. G. Single phase flow pressure drop and heat transfer in rectangular metallic microchannels. *Applied Thermal Engineering*. 2016, 93, 1324-1336.

Sahar, A. M.; Wissink, J.; Mahmoud, M. M.; Karayiannis, T. G.; Ishak, M. S. A. Effect of hydraulic diameter and aspect ratio on single phase flow and heat transfer in a rectangular microchannel. *Applied Thermal Engineering*. 2017, 115, 793-814.

Saw, L. H.; Ye, Y.; Tay, A. A. O.; Chong, W.T.; Kuan, S. H.; Yew, M.C. Computational fluid dynamic and thermal analysis of Lithium-ion battery pack with air cooling. *Applied Energy*. 2016, 177, 783-792.

Şen S.; Darici S. Transient conjugate heat transfer in a circular microchannel involving rarefaction, viscous dissipation and axial conduction effects. *Applied Thermal Engineering*. 2017, 111, 855-862.

Shafahi, M.; Bianco, V.; Vafai, K.; Manca, O. Thermal performance of flat-shaped heat pipes using nanofluids. *Int. J. Heat Mass Transfer*. 2010, 53(7-8), 1438-1445.

Shen, S.; Xu, J. L.; Zhou, J. J.; Chen, Y. Flow and heat transfer in microchannels with rough wall surface. *Energy Conversion and Management*. 2006, 47, 1311-1325.

Steinke M. E.; Kandlikar, S. G. Single-phase liquid friction factors in microchannels. *Int. J. Thermal Sciences*. 2006, 45, 1073-1083.

Sun, H.; Faghri, M. Effect of Surface Roughness on Nitrogen Flow in a Microchannel Using the Direct Simulation Monte Carlo method. *Numerical Heat Transfer: Part A: Applications*. 2003, 43(1), 1-8, 2003.

Smith, K.; Wang, C. Y. Power and thermal characterization of a lithium-ion battery pack for hybrid-electric vehicles. *J. Power Sources*. 2006, 160, 662-673.

Tan, S. T.; Ng, E. Y. K. Numerical Analysis of EDL Effect on Heat Transfer Characteristic of 3-D Developing Flow in a Microchannel. *Numerical Heat Transfer, Part A: Applications*. 2006, 49(10), 991-1007.

Teng, H.; Yeow, K. Design of Direct and Indirect Liquid Cooling Systems for High Capacity, High-Power Lithium-Ion Battery Packs. *SAE Int. J. Alternative Powertrains*. 2012, 1, 525-536.

Tong, W.; Somasundaram, K.; Birgersson, E.; Mujumdar, A.S.; Yap, C. Numerical investigation of water cooling for a lithium-ion bipolar battery pack. *Int. J. Thermal Sciences*. 2015, 94, 259-269.

Tuckerman, D.B.; Pease, R.F.W. High-performance heat sinking for VLSI. *IEEE Electronic Device Letters*. 1981, 5, 126-129.

Vajdi, M.; Moghanlou, F.S.; Niari, E.R.; Asl, M.S.; Shokouhimehr, M. Heat transfer and pressure drop in a ZrB_2 microchannel heat sink: A numerical approach. *Ceramics Int*. 2020, 46, 1730-1735.

Vertiz G. et al. Thermal characterization of large size lithium-ion pouch cell based on 1d electro-thermal model. *J. Power Sources*. 2014, 272, 476-484.

Wang, C.; Zhang, G.; Meng, L.; Li, X.; Sit, W.; Lv, Y.; Rao, M. Liquid cooling based on thermal silica plate for battery thermal management system. *Int. J. Energy Research*. 2017, 41, 2468–2479.

Wang, T.; Tseng, K. J.; Zhao, J. Development of efficient air-cooling strategies for lithium-ion battery module based on empirical heat source model. *Applied Thermal Engineering*. 2015, 90, 521–529.

Weilin, Q.; Mala G. M.; Dongqing, L. Pressure-driven water fows in trapezoidal silicon microchannels. *Int. J. Heat Mass Transfer*. 2000, 43, 353-364.

Wu, H. Y.; Cheng, P. An experimental study of convective heat transfer in silicon microchannels with different surface conditions. *Int. J. Heat Mass Transfer*. 2003, 46, 2547-2556.

Wu, P. Y.; Little, W. A. Measurement of friction factors for the flow of gases in very fine channels used for micro-miniature Joule–Thomson refrigerators. *Cryogenics*. 1983, 273-277.

Xiao, M., Choe, S.Y. Theoretical and experimental analysis of heat generations of a pouch type LiMn2O4/carbon high power Li-polymer battery. *J. Power Sources*. 2013, 241, 46-55.

Xie, Y.; Shi, S.; Tang, J.; Wu, H.; Yu, J. Experimental and analytical study on heat generation characteristics of a lithium-ion power battery. *Int. J. Heat Mass Transfer*, 2018, 122, 884-894.

Xu, B.; Ooi, K. T.; Wong, N. T.; Choi, W. K. Experimental Investigation of Flow Friction for Liquid Flow in Microchannels. *Int. Communications Heat Mass Transfer*. 2000, 27(8), 1165-1176.

Xu, J.; Lan, C.; Qiao, Y.; Ma, Y. Prevent thermal runaway of lithium-ion batteries with minichannels cooling. *Applied Thermal Engineering*, 2017, 110, 883-890.

Xuan, Y.; Li, Q.; Hu, W. Aggregation structure and thermal conductivity of nanofluids. *AIChE J*. 2003, 49(4), 1038–1043.

Xun, J.; Liu, R.; Jiao, K. Numerical and analytical modeling of lithium ion battery thermal behaviors with different cooling designs. *J. Power Sources*., 2013, 233, 47-61.

Yadav, V.; Baghel, K; Kumar, R; Kadam, S. T. Numerical investigation of heat transfer in extended surface microchannels. *Int. J. Heat Mass Transfer*. 2016, 93, 612-622.

Yang, C.; Li, D. Analysis of electrokinetic effects on the liquid flow in rectangular microchannels. *Colloids and Surfaces A: Physicochemistry Engineering Aspects*. 1998, 143, 339-353.

Yeow, K.; Teng, H.; Thelliez, M.; Tan, E. Thermal Analysis of a Li-ion Battery System with Indirect Liquid Cooling Using Finite Element Analysis Approach. *SAE Int. J. Alternating Power*. 2012, 1, 65-78.

Yi, J.; Kim, U. S.; Shin, C. B.; Han, T.; Park, S. Three-Dimensional Thermal Modeling of a Lithium-Ion Battery Considering the Combined Effects of the Electrical and Thermal Contact Resistances between Current Collecting Tab and Lead Wire. *J. The Electrochemical Society*. 2013, 160, A437-A443.

Yu, F.; Wang T.; Zhang, C. Effect of axial conduction on heat transfer in a rectangular microchannel with local heat flux. *J. Thermal Science and Technology*, 2018, 17-00551, 1-13.

Yuan, X; Tao, Z; Li, H; Tian, Y. Experimental investigation of surface roughness effects on flow behavior and heat transfer characteristics for circular microchannels. *Chinese J. Aeronautics*. 2016, 29(6), 1575-1581.

Yuan, F.; Lin, J.; Ku, X. Convective heat transfer and resistance characteristics of nanofluids with cylindrical particles. *Heat Transfer Engineering*. 2018, 39(6), 526–535.

Zhai, Y.; Xia, G.; Li, Z.; Wang, H. Experimental investigation and empirical correlations of single and laminar convective heat transfer in microchannel heat sinks. *Experimental Thermal and Fluid Science*. 2017, 83, 207-214.

Zhang, X.; Zhao, T.; Wu S.; Yao, F. Experimental Study on Liquid Flow and Heat Transfer in Rough Microchannels. *Advances in Condensed Matter Physics Volume*. 2019, 1974952, 1-10.

Zhao, H.; Raghunandanan, S.; Elbel; S.; Hrnjak, P. A Study of Microchannel Heat Exchanger Performance Associated with the Manufacturing Process. *Int. Refrigeration and Air Conditioning Conference*, 2016, Paper 1789.

Zhao, R.; Gu, J.; Liu, J. An experimental study of heat pipe thermal management system with wet cooling method for lithium ion batteries. *J. Power Sources*. 2015, 273, 1089-1097.

Zhang, S. X.; He, Y.L.; Lauriat, G.; Tao, W.Q. Numerical studies of simultaneously developing laminar flow and heat transfer in microtubes with thick wall and constant outside wall temperature. *Int. J. Heat Mass Transfer*. 2010, 53, 3977-3989.

Zhang, X.; Zhao, T.; Wu, S.; Yao, F. Experimental study on liquid flow and heat transfer in rough microchannels. *Advenced Conden Matterial Physics*. 2019, 1974952, 1-9.

Zhimin, W.; Fah, C. K. The Optimum Thermal Design of Microchannel Heat Sinks. In *Proceeding of IEEUCPMT Electronic Packaging Technology Conference*. 1997, 123-129.

Zhou, G.; Yao, S. C. Effect of surface roughness on laminar liquid flow in micro-channels. *Applied Thermal Engineering*. 2011, 31, 228-234.

VITA

Turgay COŞKUN

2013	B.S. degree in Mechanical Engineering Department, Izmir Institute of Technology, Turkey
2016	M.S. degree in Energy Systems Engineering Department, Izmir Institute of Technology, Turkey

FIELD OF STUDY

Heat Transfer in Microchannels, Cooling of Battery Cells, Thermodynamics

PUBLICATIONS

Turgay Coşkun, Erdal Çetkin, "A review of heat and fluid flow characteristics in microchannel heat sinks", Heat Transfer, Vol. 49, pp .4109–4133, 2020.
DOI: 10.1002/htj.21819.

Turgay Coşkun, Erdal Çetkin, "Heat Transfer Enhancement in a Microchannel Heat Sink: Nanofluids and/or Micro Pin Fins", Heat Transfer Engineering, Vol. 41, No. 21, pp. 1818-1828, 2020.
DOI: 10.1080/01457632.2019.1670467.

Turgay Coşkun, Erdal Çetkin, "Elektrikli Araç Batarya Hücresinin Mikrokanallı ısı değiştiricisi ile ısıl yönetimi", ULIBTK'21 Uluslararası Katılımlı 23. Isı Bilimi ve Tekniği Kongresi, 08-10 Eylül 2021, Gaziantep, Türkiye